Simulation study for the Stratospheric Inferred Winds (SIW) sub-millimeter limb sounder

Philippe Baron[1], Donal Murtagh[2], Patrick Eriksson[2], Jana Mendrok[2,3], Satoshi Ochiai[1], Kristell Pérot[2], Hideo Sagawa[4], and Makoto Suzuki[5]

[1]National Institute of Information and Communications Technology, 4-2-1 Nukui-kitamachi, Koganei, Tokyo 184-8795, Japan
[2]Department of Space, Earth and Environment, Chalmers University of Technology, 41296 Göteborg, Sweden
[3]At Chalmers University of Technology until Dec. 2017
[4]Kyoto Sangyo University, Kyoto, Japan
[5]Japan Aerospace Exploration Agency, Tsukuba, 305-8505 Japan

Correspondence to: P. Baron (baron@nict.go.jp)

Abstract. Stratospheric Inferred Winds (SIW) is a Swedish mini sub-millimeter limb sounder selected for the 2nd InnoSat platform, with a launch planned for near 2022. It is intended to fill the altitude gap between 30–70 km in atmospheric wind measurements and also aims at pursuing the limb observations of temperature and key atmospheric constituents between 10–90 km when current satellite missions are probably stopped. Line-of-sight winds are retrieved from the Doppler shift of molecular emission lines introduced by the wind field. Observations will be performed with two antennas pointing toward the limb with perpendicular directions in order to reconstruct the 2-D horizontal wind vector. Each antenna has a vertical field of view of 5 km. The chosen spectral band, near 655 GHz, contains a dense group of strong O_3 lines suitable for exploiting the small amount of wind information in stratospheric spectra. Using both sidebands of the heterodyne receiver, a large number of chemical species will be measured including O_3-isopotologues, H_2O, HDO, HCl, ClO, N_2O, HNO_3, NO, NO_2, HCN, CH_3CN and HO_2. This paper presents a simulation study for assessing the measurement performances. The line-of-sight winds are retrieved between 30–90 km with the best sensitivity between 35–70 km where the precision (1-σ) is 5–10 $\mathrm{m\,s^{-1}}$ for a single scan. Similar performances can be obtained during day and night conditions except in the lower mesosphere where the photo-dissociation of O_3 in day-time reduces the sensitivity by 50 % near 70 km. Profiles of O_3, H_2O and temperature are retrieved with a high precision up to 50 km (< 1 %, < 2 %, 1 K, respectively). Systematic errors due to uncertainties on spectroscopic parameters, on the radiometer sideband ratio and in the radiance calibration process are investigated. A large wind retrieval bias of 10–30 $\mathrm{m\,s^{-1}}$ between 30–40 km can be induced by the air-broadening parameters uncertainties of O_3 lines. This highlights the need for a good knowledge of these parameters and for study of methods to mitigate the retrieval bias.

1 Introduction

Millimeter and sub-millimeter (MM and SMM) limb sounders have been successfully used for more than two decades to probe the atmospheric composition and the temperature from the upper-troposphere to the lower thermosphere (Waters et al., 1993; Murtagh et al., 2002; Waters et al., 2006; Kikuchi et al., 2010). The first generation of Millimeter Limb Sounder (MLS)

provided unique observations of ClO, O_3, H_2O and HNO_3 allowing, for instance, a better understanding of the physical and chemical processes leading to the northern high-latitude O_3 depletion (Waters et al., 1993). Subsequent SMM missions have allowed the monitoring of the middle-atmosphere (15–110 km) almost without interruption since the first MLS and have significantly contributed to the current middle-atmospheric measurement database (Hegglin and Tegtmeier, 2017). However, no successors of these missions are planned yet, and there is a risk of an observation gap in the near future (Livesey and Santee, 2017).

The advantages of such observations are manifold. The thermal emission spectrum at MM and SMM wavelengths is rich in isolated spectral lines from asymmetric molecules and molecular oxygen. Some important chemical species, such as HO_2 and ClO, have their clearest signals in this region of the spectrum (Urban et al., 2005; Khosravi et al., 2013; Sagawa et al., 2013; Millán et al., 2015). The O_2 lines give temperature and pressure, and the limb geometry provides a suitable vertical resolution for describing the middle-atmosphere. Molecules are sensed in the thermal equilibrium state with no diurnal difference in the measurement performance, and measurements are not perturbed by stratospheric polar-clouds and aerosols. Furthermore, the technology is mature allowing missions to operate over a period longer than a decade. Methods have already been used for improving the horizontal resolution with tomographic observations (Livesey et al., 2006; Christensen et al., 2015) or for obtaining very high signal-to-noise ratio using 4-K cryogenic cooling (Kikuchi et al., 2010).

Modeling middle-atmospheric major dynamical phenomena such as vertically propagating tidal waves, high-latitude sudden-stratospheric warming or equatorial quasi-biennial oscillation are still challenging (Limpasuvan et al., 2012; Newman et al., 2016; Orsolini et al., 2017; Sakazaki et al., 2018). Wind is one of the primary parameters for describing the physical state of the atmosphere but models have difficulties in reproducing it where the atmospheric flow cannot be described by the geostrophic approximation, such as in the equatorial region where the Coriolis force is weak and, in the upper stratosphere and mesosphere where waves and tides tend to dominate the wind fields (Baron et al., 2013b; Le Pichon et al., 2015; Kawatani et al., 2016; Duruisseau et al., 2017; Rüfenacht et al., 2017). As climate and weather models increase their vertical range to encompass more of the stratosphere and mesosphere, the need for measurements to improve the accuracy of models in this region, and hence at lower altitudes, can be expected to rise (Baldwin et al., 2003; Hoppel et al., 2008; Baldwin et al., 2010; Gerber et al., 2012). Only High Resolution Doppler Imager (HRDI) on Upper Atmospheric Research Satellite (1991–2005) has been able to measure horizontal winds over the stratosphere and mesosphere (Ortland et al., 1996), and current spaceborne sensors are not able to measure wind accurately below 90 km (Shepherd, 2015). Ground-based stations do not cover the globe uniformly and most of the data are limited to heights below 30 km (Ishii et al., 2017) or above 70 km (Baumgarten, 2010). However recent efforts have been made to close this altitude gap (Baumgarten, 2010; Rüfenacht et al., 2014; Le Pichon et al., 2015; Blanc et al., 2018).

Providing wind data in the middle atmosphere from space is one of the challenges for future missions. The European Space Agency is going to launch this year the Atmospheric Dynamics Mission equipped with a wind lidar to demonstrate the feasibility of such measurements (Stoffelen et al., 2005). However a lidar is well suited for measuring wind in the troposphere but has poor precision above 20–30 km (Ishii et al., 2017). The Stratospheric Wind Interferometer For Transport studies

(SWIFT) has been studied by the Canadian Space Agency for deriving winds between 15–45 km from O_3 infra-red emission lines (Rahnama et al., 2013). The mission was originally planned for 2010 but it is now very uncertain.

The potential of MM/SMM limb sounders for measuring winds has been demonstrated with line-of-sight wind retrievals between 70–90 km from the MLS O_2 line (Wu et al., 2008) and between 30–80 km from O_3 and HCl lines measured with Superconducting Submillimeter-Wave Limb-Emission Sounder (SMILES) (Baron et al., 2013b). Wind is one of the main outcomes of SMILES-2 that is proposed to the Japan Aerospace Exploration Agency (JAXA) (Ochiai et al., 2017). It is a large instrument (>500 kg) using cryogenic SMM and THz receivers designed for very high sensitive observations between 15–150 km. If it is selected this year, the launch will be near 2025. Two smaller missions are studied with the possibility to be launched as soon as 2020–22. Wu et al. (2016) propose a small instrument for measuring the atomic oxygen line at 2.06 THz in order to retrieve its abundance as well as temperature and wind in the lower thermosphere. However this mission cannot provide stratospheric and lower mesospheric information. The second proposal is Stratospheric Inferred Winds (SIW). It is a small and low-cost satellite mission studied within the Swedish Innosat program (Lindberg, 2016; Murtagh, 2016). Through this program, it is planned to launch a scientific mission every two years, and SIW has been selected for the 2nd launch near 2022. It will observe the middle-atmosphere (15–90 km) for a period expected to be at least 2 years, and will provide horizontal-wind vector within 30–90 km. The other primary products are the profiles of temperature, O_3, H_2O and more than a dozen of other chemical species. With this mission it will be possible to ensure the continuous monitoring of the middle-atmosphere avoiding a SMM measurement gap.

In this paper we present a simulation study to assess the potential of SIW. A special focus is put on the main parameters: wind, temperature, O_3 and H_2O that are derived from the strongest lines in the selected spectral bands. Section 2 describes the mission and the observation technique. The measurement simulation and the retrieval method are explained in Sect. 3 and 4, respectively. The measurement performances are discussed in Sect. 5 and concluding remarks are given in the final section.

2 Mission description

2.1 Observation and instrument characteristics

The scientific payload (Fig. 1) and observations characteristics are summarized in Table 1. This is the proposed setting which can still be slightly modified. The platform will be set on a sun-synchronous polar orbit at an altitude of 550 km. It will fly near the terminator crossing the equatorial ascending node at 18:00 local-time (LT). Atmospheric observations will be performed toward the night side using two antennas looking perpendicularly to each other with angles from the satellite velocity of 45° and 135°, respectively. The antennas will point toward close air-masses with few minutes delay (Fig. 2). They are fixed on the platform and the whole satellite will nod up and down in order to scan the limb alternatively upward and downward from about 15 to 90 km. The forward antenna is used during the upward scans and the aftward one during the downward scans. With this choice, the horizontal displacement of the tangent point during a vertical scan is less than 300 km, the vertical motion of the line-of-sight partly counterbalancing the satellite motion. Using the line-of-sight (LOS) winds retrieved with the two antennas
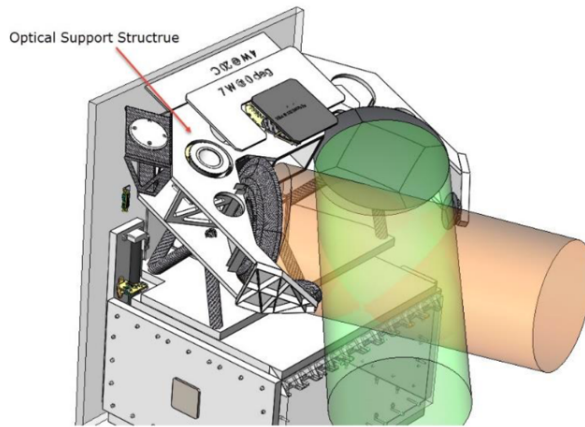
Figure 1. View of the Innosat satellite. The box in the lower-part is the platform service module. Above it is the scientific payload including the two antennas. The field of views are represented with green and beige colors (from Omnisys instruments co).

over close regions allows us to derive the meridional and zonal wind components (Appendix A). The separation between the LOS wind profiles is less than 400 km.

The signals from the antennas are alternatively sent to a single radiometer passively cooled to 70 K below the ambient temperature, and analysed with an auto-correlator spectrometer. The heterodyne radiometer operates in double-sideband (DSB)

5   mode yielding to the superposition in the measured spectrum of the two image bands with respect to the local oscillator. The bandwidth and resolution are 8 GHz and 1 MHz, respectively.

The strategy for acquiring the calibration data is not definitively decided yet and will probably be optimized in the future. Currently the plan is as follows. A calibration load onboard the plaform (black body at ambient temperature) is viewed at the bottom and top of each scan during the turnaround. While limb scanning, the atmosphere and cold-sky are observed

10   alternatively with an integration time of 0.5 s each. Hence, atmospheric spectra are obtained every 2.3 km with an effective vertical resolution of about 5 km.

2.2   Spectral bands

The measured spectrum is composed of molecular lines spectrally resolved (Fig. 3). Using a radiative transfer model, they are inverted to retrieve geophysical information. Volume mixing ratio (VMR) and temperature are retrieved from their amplitude,

15   whereas tangent-height pressure and line-of-sight wind are retrieved from the width and the frequency position of the lines, respectively.

The Doppler shift induced by the LOS wind (2 kHz for $1 \mathrm{\,m\,s^{-1}}$) is small compared to the line broadening ($1 - 100$ MHz). This gives a very weak signal to exploit, especially in the lower stratosphere. Baron et al. (2013a) have shown that the spectral region near 655 GHz is the most suitable one for measuring wind with the current hardware. It contains a dense group of

4

Table 1. Characteristics of the SIW payload and observations. The relationship between tangent-height and LOS angle is derived for an Earth radius of 6370 km and a satellite altitude of 550 km above the geoid.

Payload volume	$40 \times 70 \times 40$ cm^3
Payload mass/power	17 kg/47 W
Antenna diameter	30 cm
Satellite altitude	500–600 km
Orbit inclination	98 ° (sun synchronous)
Latitude range	65 °S–82 °N
Local time of ascending node	18:00
Scan altitude	10–90 km
LOS nadir angle	67.25–69.03 ° (1.78 °)
Scan velocity	$0.05 \,°\,\text{s}^{-1}$ (35 s/scan)
Spectrum integration time	0.5 s (1.14 km*)
Antenna vertical FOV	5 km
DSB system temperature	1000–1200 K
ACS Bandwidth	8 GHz
ACS resolution	1 MHz
LO frequency	638.075 GHz ($\lambda = 0.47$ mm)
IF frequency	10.975–18.975 GHz
Frequency $\Leftrightarrow$ velocity	$1 \,\text{m s}^{-1} \Leftrightarrow 2$ kHz

* Tangent point vertical displacement

strong O_3 lines (second row of Fig. 3), that increases by at least a factor 2 the wind measurement sensitivity between 40–70 km compared to retrievals performed from a band with similar characteristics but located at any other frequency under 800 GHz. This band also allows us to retrieve temperature with a good precision in the stratosphere without measuring an O_2 line.

The local-oscillator frequency has been carefully selected in order to include as many as possible spectral lines and to reduce the line superposition from both sidebands. Hence lines of chemical species such as HCN (620.3 GHz), H^{37}Cl (625.0 GHz) H^{35}Cl (625.9 GHz), ^{35}ClO (649.5 GHz), NO (651.1 GHz) and N_2O (652.8 GHz) are clearly visible. A strong H_2O line is located at 620.7 GHz but very close to an O_3 line with similar strength. Lines from around twenty molecules are available though some are very weak such as H_2CO, CH_3Cl or BrO. Finally let's note that most of the lines where IF > 14 GHz have already been measured with Aura MLS and JEM/SMILES.
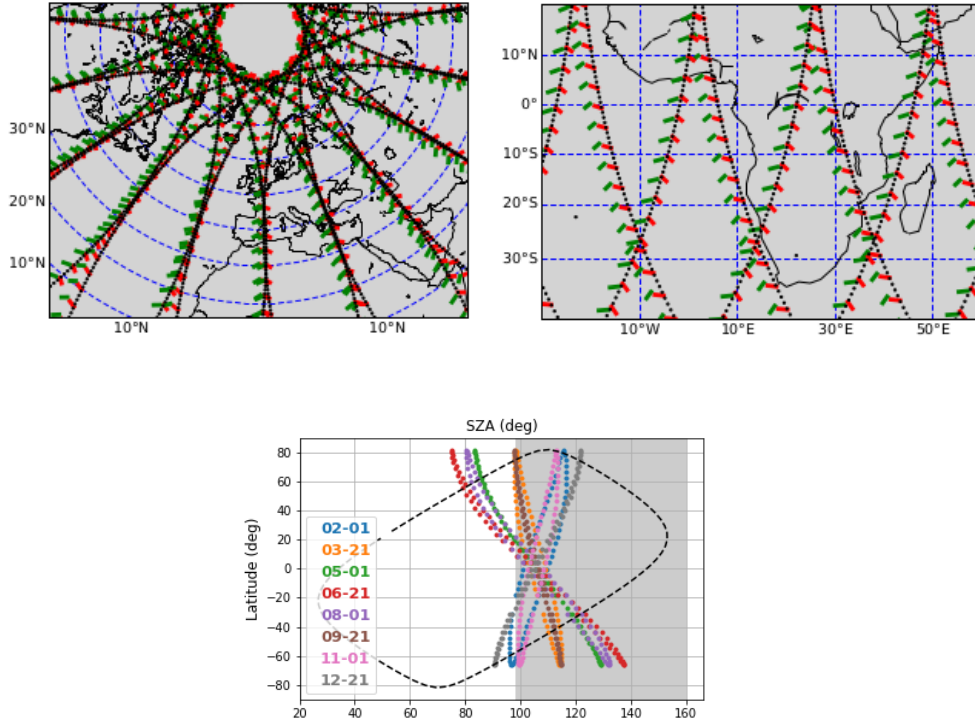
Figure 2. The upper panels show the footprints of the forward (45°) and aftward (135°) views over a 24-hour period. the forward antenna is used during the upward scans (red lines) and the aftward one during the downward scans (green lines). The first tangent point of the upward-scans are located on the black-dotted lines. The lower panel shows the solar zenith angles with respect to latitudes for various days representative of the seasonal variation (colored dots) together with those of the Aura MLS data (DJF, 2011) used in the simulations (dashed line). The shaded area shows the nighttime measurements in the mesosphere where the O_3 diurnal variation is the strongest.

3 Measurement modeling

3.1 Radiative transfer and instrument

The signal is a spectral and spatial average of specific intensities ($\mathrm{W\,m^{-2}\,sr^{-1}\,Hz^{-1}}$) over narrow instrumental functions. It is expressed in the so-called Rayleigh-Jeans brightness temperature T_b equal to (Urban et al., 2004)

$$
T_\mathrm{b}\,(\theta_j,\,\vartheta_k) = \kappa_b \int\limits_{\Delta\vartheta} d\vartheta \quad g^\mathrm{sp}\,(\vartheta - \vartheta_k) \left\{ w_\mathrm{lsb}(\vartheta) \int\limits_{\Delta\theta} G_\mathrm{e}^\mathrm{ant}\,(\theta - \theta_j,\,\nu_\mathrm{lo} - \vartheta)\,I(\theta,\nu_\mathrm{lo} - \vartheta)\,d\theta \right.
$$
$$
\left. + (1 - w_\mathrm{lsb}(\vartheta)) \int\limits_{\Delta\theta} G_\mathrm{e}^\mathrm{ant}\,(\theta - \theta_j,\,\nu_\mathrm{lo+\vartheta})\,I(\theta,\nu_\mathrm{lo} + \vartheta)\,d\theta \right\},
$$

(1)

where ϑ_k is the frequency of the kth spectral component of the measurement, θ_j is the mean nadir angle during the measurement integration time of the jth spectra of the scan, and I is the specific intensity. The specific intensity is integrated along a LOS as
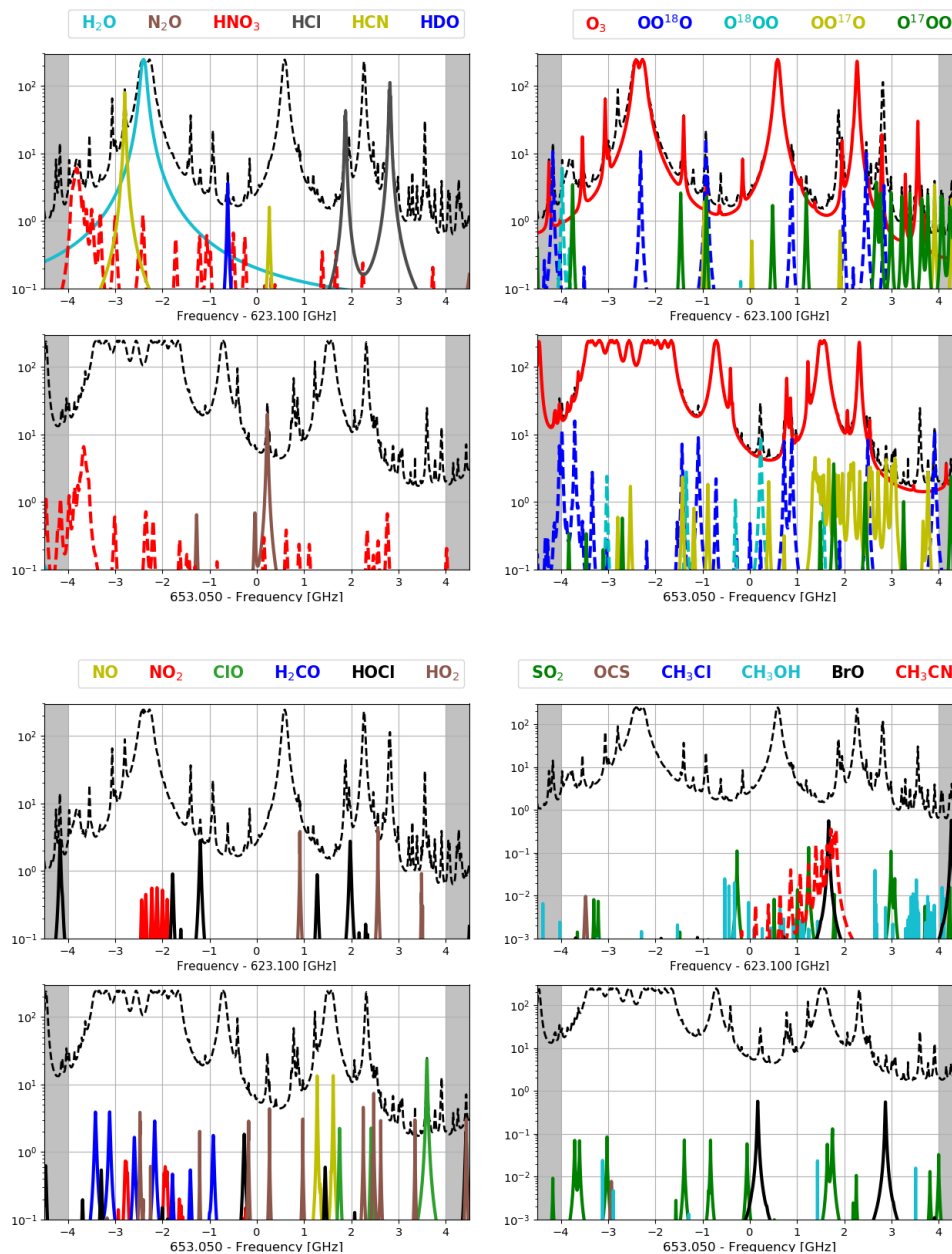
Figure 3. Contribution of the most relevant chemical species to the SIW spectrum. More that 20 molecules are shown in 4 groups of two panels. In each group, the upper panel shows the lower sideband spectrum (dashed black lines) with a central frequency of 623.1 GHz and the lower panel shows the upper sideband one with a central frequency of 653.05 GHz. The colored lines are single-molecule spectra. Grey-shaded areas are outside the bandwidth. The tangent height is 35 km and frequencies are ordered according to the intermediate frequencies. The intensity is given in brightness temperature (y-axis).

7

that shown in Fig. 4. The LOS is characterized by the altitude of the tangent point, the angle with the meridional direction ϕ_n and narrow ranges over which the atmopshere is considered homogeneous. The heterodyne receiver is sensitive to atmospheric radiation at frequencies $\nu_{lo} \pm \vartheta$ where ν_{lo} and ϑ are the local-oscillator and intermediate frequencies (Tab. 1). The instrumental functions are the spectrometer channel response g_{sp} (Hz^{-1}), the relative weight of the radiometer sidebands w_{lsb}, and the effective antenna pattern G_e^{ant}. The parameter κ_b is the Rayleigh-Jeans factor, used to convert the intensity into brightness temperature:

$$\kappa_b = \frac{c^2}{2\,k_b\,\nu_{lo}^2},$$

where $c = 2.997924 \times 10^8$ m s^{-1} is the speed of light in vacuum and $k_b = 1.380662 \times 10^{-23}$ J K^{-1} the Boltzmann constant. The spectrometer channel response is assumed to be Gaussian with a Full-Width-Half-Maximum (FHWM) of 1 MHz. Given that the altitude range scanned during the spectrum integration is small compared to the static-antenna vertical resolution (1.1 km and 5 km, respectively), the effective antenna pattern including the vertical scan, is approximated by a Gaussian function with the FWHM:

$$\sigma_e^{ant} = \sqrt{\left(\frac{1.22}{D}\frac{c}{\nu_{lo}}\right)^2 + \left(\dot{\theta}\Delta_T\right)^2}, \qquad (2)$$

where D (m) is the antenna diameter, $\dot{\theta}$ (rad s^{-1}) is the vertical scan velocity and Δ_T is the spectrum integration time. The antenna sidelobes are also neglected. These approximations have negligible impacts on this study. A constant spectral sideband weight is used, $w_{lsb}(\vartheta) = 0.5$. The integrals in Eq. (1) are computed over ranges $\Delta\theta$ and $\Delta\vartheta$ set to 3 times the FWHM of their corresponding response functions.
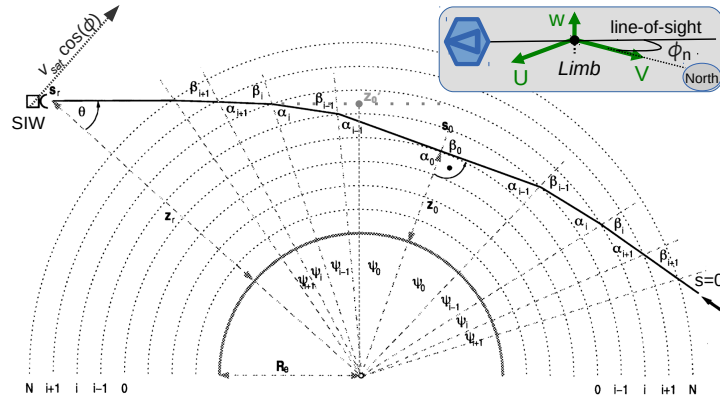

Figure 4. Limb sounding geometry for a refracted line-of-sight (full line) and a none refracted one (dashed line). The panel on the right-upper corner shows the orientation of the LOS with respect to the wind components at the tangent point. Figure is adapted from Urban et al. (2004).

3.2 Specific intensity and wind

The specific intensity is computed using the radiative transfer equation:

$$I(\theta,\nu) = \int\limits_{s=0}^{s_r} B_\nu(s)\, K_\nu\left(s, \{\nu_a(s)\}_{\text{lines}}\right) \exp\left(-\int\limits_{s'=s}^{s_r} K_\nu\left(s, \{\nu_a(s')\}_{\text{lines}}\right) ds'\right) ds, \tag{3}$$

where s indicates the position on the LOS, B is the Planck function ($\mathrm{W\,m^{-2}\,sr^{-1}\,Hz^{-1}}$) and K ($\mathrm{m^{-1}}$) is the absorption coefficient. The background cosmic radiation ($T_b \approx 1$ mK) is neglected. The absorption coefficient is computed with a line-by-line and continua models (Urban et al., 2004). The spectroscopic parameters describing the molecular lines are taken from the HITRAN catalog (Rothman et al., 2009) except those for BrO, CH_3Cl and CH_3CN which are not available in HITRAN and are, then, taken from the Jet Propulsion Laboratory catalog (Pickett et al., 1998). The frequency of the spectral lines viewed from the receiver ($\{\nu_a(s)\}_{\text{lines}}$) depends on the mean relative motion of the molecules with respect to the receiver, i.e., satellite velocity and wind. The Doppler-shift effect on the Planck function is neglected. The line frequency is also shifted by the atmospheric pressure but this effect is small above 25 km where winds are measured. For the H2O line at 620 GHz, 2% error on the shift parameter corresponds to an error of $2\,\mathrm{m\,s^{-1}}$ at 10 hPa. The shift on O_3 lines should be smaller but the information is not available in HITRAN and further studies are needed to infer it.

A spherical Earth is assumed for assessing the impacts of all the parameters contributing to the line Doppler shift. At a height z_i and for a LOS nadir angle θ, the line apparent frequency is (Kursinski et al., 1997)

$$\nu_a(\theta,z_i) = \nu_0\left(1 - \frac{\left[V(z_i)\cos(\phi_n) + (U(z_i)+\omega_e R_e \cos(\Lambda))\sin(\phi_n)\right]\sin(\alpha_i)}{c} + \frac{W\cos(\alpha_i)}{c} + \frac{V_{\text{sat}}\cos(\phi)\sin\theta}{c}\right) \tag{4}$$

where ν_0 (Hz) is the rest frequency of the transition, V_{sat} is the satellite velocity with respect to a fixed frame attached to the Earth center, (U, V, W) is the 3-D wind velocity defined with respect to the Earth surface, and ω_e, Λ and Re are the Earth rotation angular velocity ($\mathrm{rad\,s^{-1}}$), the latitude and the geoid radius at the position i. The LOS nadir angle at z_i is α_i, and ϕ_n is the angle between the LOS and the north direction (Fig. 4). At the tangent height point ($i = 0$), $\alpha_0 = 90°$ and the Doppler shift $\delta\nu(\theta,z_0)$ is

$$\delta\nu(\theta,z_0) = -\frac{\nu_0}{c}\left(V_{\text{los}}(z_0) + \omega_e R_e \cos(\Lambda)\sin(\phi_n) - V_{\text{sat}}\cos(\phi)\, n_0 \frac{z_0 + R_e}{z_r + R_e}\right), \tag{5}$$

where z_r is the receiver height, n_0 is the refractive index at the tangent point, $\sin(\theta) = n_0 \frac{z_0 + R_e}{z_r + R_e}$ and V_{los} is the LOS component of the horizontal wind:

$$V_{\text{los}}(z_0) = V(z_0)\cos(\phi_n) + U(z_0)\sin(\phi_n). \tag{6}$$

At the equator and for the forward LOS, the Doppler shifts due to the satellite velocity and to the Earth rotation are ≈ -8 MHz ($+4000\,\mathrm{m\,s^{-1}}$) and ∓ 0.74 MHz ($\pm 370\,\mathrm{m\,s^{-1}}$), respectively. In order to simplify the calculations, we consider the case of a pseudo LOS-wind profile which, unlike a real one, induces a Doppler-shift $\delta\nu(z) = -\nu_0/c\, V_{\text{plos}}(z)$ that is independent of the angles α_i and Earth rotation, and includes the vertical changes due to the satellite velocity:

$$V_{\text{plos}}(z) = V_{\text{los}}(z) - V_{\text{sat}}\cos(\phi)\, n_z\left(\frac{z - 50\text{ km}}{z_r + R_e}\right). \tag{7}$$

9

At the tangent point, the pseudo wind induced the same Doppler-shift as that given in Eq. (5) to within the same constant over the full vertical scan. The constant includes the Earth rotation effects and most of the satellite velocity ones. The terms embedded in this constant are known with a precision better than $1 \, \mathrm{m \, s^{-1}}$ using the star-trackers and GPS data onboard the satellite. Such a setting is chosen to yield the satellite-velocity induced Doppler-shift to zero at $z = 50 \, \mathrm{km}$, center of the vertical scan.

The pseudo-wind approximation induces errors on the line apparent frequency at positions on the LOS other than the tangent point. These errors are smaller than $10 \, \mathrm{cm \, s^{-1}}$ and have negligible impacts on the retrievals. Indeed, VMR and temperature retrievals are not sensitive to small frequency errors, and regarding wind retrieval, the information is extracted from optically thin measurements which are characterized by narrow specific-intensity weighting functions peaking at the tangent point.

3.3   Calibration and measurement noise

The raw intensity delivered by the spectrometer is expressed as (Olberg et al., 2003):

$$C_{i,j} = G_{i,j} \left[T_{sys}(i,j) + \eta_x \, T_b(i,j) + (1 - \eta_x) \, T_{so}(i) \right] \tag{8}$$

with i and j are the tangent height and frequency indices, T_{sys} is the double sideband system temperature, T_{so} is the mean brightness-temperature introduced by the optics spillover, η_x is the efficiency of the integrated antenna (x=a) or hot-load horn (x=c), and G is the radiometric gain. The last is

$$G_{i,j} = g_{i,j} \left(1 - \alpha \langle C_{i,j} \rangle \right) \tag{9}$$

where $\langle \bullet \rangle$ denotes the average over the frequencies j and α is a positive coefficient to account for a non-linear response of the radiometer (Ochiai et al., 2013). The double-sideband system temperature of SIW is expected to be about 1100 K (OMNISYS, private communication). The signal intensity is calibrated using the emissions from the cold sky with a Rayleigh-Jeans temperature $T_c \approx 10^{-3}$ K, and from an ambient temperature hot-load (Rayleigh-Jeans temperature $T_h \approx 250$ K) measured between two scans. Assuming a linear response of the radiometer and using $T_c \ll T_h$, the radiometer gain is derived as (Olberg et al., 2003)

$$\widehat{G}_j = \frac{\overline{C}_h(j) - \overline{C}_c(j)}{\epsilon \, T_h}, \tag{10}$$

where ϵ is the hot-load emissivity, and C_h and C_c are the receiver raw outputs for the hot load and cold-sky. The upper-bars $\overline{\bullet}$ indicate that an average value over the whole scan is used. The brightness temperature of the atmospheric signal is then

$$\widehat{T}_b(i,j) = \frac{C_{atm}(i,j) - \overline{C}'_c(i,j)}{\eta_a \widehat{G}_{i,j}} + \mathrm{offset}_i, \tag{11}$$

where C_{atm} is the receiver output when the atmosphere is viewed and $\overline{C}'_c(i,j)$ is the cold sky output interpolated at the C_{atm} time. We consider that during the scan, the atmosphere and cold-sky are viewed alternatively during 0.5 sec each. The second term of the equation is a tangent-height dependent offset induced by the antenna spillover. Such radiance offset is retrieved

together with the geophysical information and it is not considered as a retrieval error source. The brightness temperature error from the radiometer noise and the calibration model is

$$
\begin{aligned}
\delta \widehat{T}_b(i,j) &= \frac{\delta C_{atm}(i,j)}{\widehat{G}_j} + \frac{\delta \overline{C}'_c(i,j)}{\widehat{G}_j} + \widehat{T}_b(i,j)\frac{\delta \widehat{G}_j}{\widehat{G}_j} + \widehat{T}_b(i,j)\frac{\delta \eta_{\mathrm{a}}}{\eta_{\mathrm{a}}} + e_{NL}(i,j) \\
&= \epsilon_{atm}(i,j) + \epsilon'_{\overline{c}}(i,j) + \left(\epsilon_{\overline{h}}(j) + \epsilon_{\overline{c}}(j)\right)\beta_h(i,j) + \left(e_{\overline{h}} + e_{\eta_{\mathrm{a}}}\right)\widehat{T}_b(i,j) + e_{NL}(i,j)
\end{aligned}
\tag{12}
$$

where ϵ_{atm} and $\epsilon'_{\overline{c}}$ are white noises on the atmospheric and cold-sky brightness temperatures (Eq. 11), $\epsilon_{\overline{c}}$ and $\epsilon_{\overline{h}}$ are those on the hot-load and cold-sky spectra in Eq. (10), and $\beta_h = \frac{T_b(i,j)}{\epsilon T_h}$. The two last elements of the equation are systematic errors induced by relative errors $e_{\overline{h}}$ and $e_{\eta_{\mathrm{a}}}$ on the hot-load emission (ϵT_H) and the antenna efficiency (η_a), and the error due to the receiver non-linearity (e_{NL}).

The noise standard-deviation is given by the radiometric equation (Jarnot et al., 2006; Ochiai et al., 2013):

$$
\sigma_t(i,j) = \left[T_{\mathrm{sys}}^{\mathrm{dsb}}(i,j) + T_{\mathrm{b}}(i,j)\right]\sqrt{\frac{1}{wt} + \left(\frac{\Delta G}{G}\right)^2},
\tag{13}
$$

where w (=1 MHz) is the noise equivalent bandwidth of spectrometer channel and t is the observation time. The term $1/wt$ describes a spectrally uncorrelated noise while $(\Delta G/G)$ describes a fully spectrally correlated noise (Jarnot et al., 2006; Ochiai et al., 2013), that is, at first approximation, a radiance offset that is mitigated by the subtraction of the cold sky in Eq. 11. Considering the average and interpolation on the cold-sky and hot loads outputs, the covariance matrix describing the measurement noise is then:

$$
\boldsymbol{S}_y(u,u') = \begin{cases}
\sigma_a^2 + \sigma_c'^2/2 + \left(\sigma_c^2 + \sigma_h^2\right)\beta_h^2(u) & \text{if } i = i' \text{ and } j = j' \\
\sigma_c'^2/2 + \left(\sigma_c^2 + \sigma_h^2\right)\beta_h(u)\beta_h(u') & \text{if } |\,i - i'\,| = 1 \text{ and } j = j' \\
\left(\sigma_c^2 + \sigma_h^2\right)\beta_h(u)\beta_h(u') & \text{if } |\,i - i'\,| > 1 \text{ and } j = j' \\
0 & \text{if } j \neq j'
\end{cases}
\tag{14}
$$

where $u = i \cdot N_f + j$ and $u' = i' \cdot N_f + j'$ and N_f the number of frequencies per spectrum. Here we consider an integration time of 2 sec for the hot load and cold sky spectra in Eq. 10 (used for assessing σ_c and σ_h). The time needed for acquiring the hot-load spectra is available between the termination of a scan and the beginning of the next one. Cold-sky spectra can be obtained in very various ways. A simple one is to construct them using the first 4 and last 4 cold-sky spectra measured during a scan.

The error e_{NL} due to the radiometer non-linear response, i.e., non-zero α in Eq. 9, is the difference between the true brightness temperature T_b and the calibrated one $\widehat{T}_b$, computed as follows (Baron et al., 2011):

1. $G_{\mathrm{cold},i,j}$ is computed applying Eq. (8) to the cold-sky view assuming $C_c = 1800$ ADU that is consistent with Odin/SMR (Olberg et al., 2003), $T_{sys} = 1100$ K, $T_b(\text{cold-sky}) = 0$ K and $\eta_x = 1$. The value $g_{i,j}$ is then computed (Eq. 9).

2. C_{hot} and C_{atm} are computed given $T_{hot} = 250$ K and T_b using an iterative process initialized with G_{cold} (Eqs. 8 and 9).

3. Finally we compute $\widehat{G}$ (Eq. 10), $\widehat{T}_b$ (Eq. 11) and $e_{NL} = \widehat{T}_b - T_b$.

4 Retrieval errors
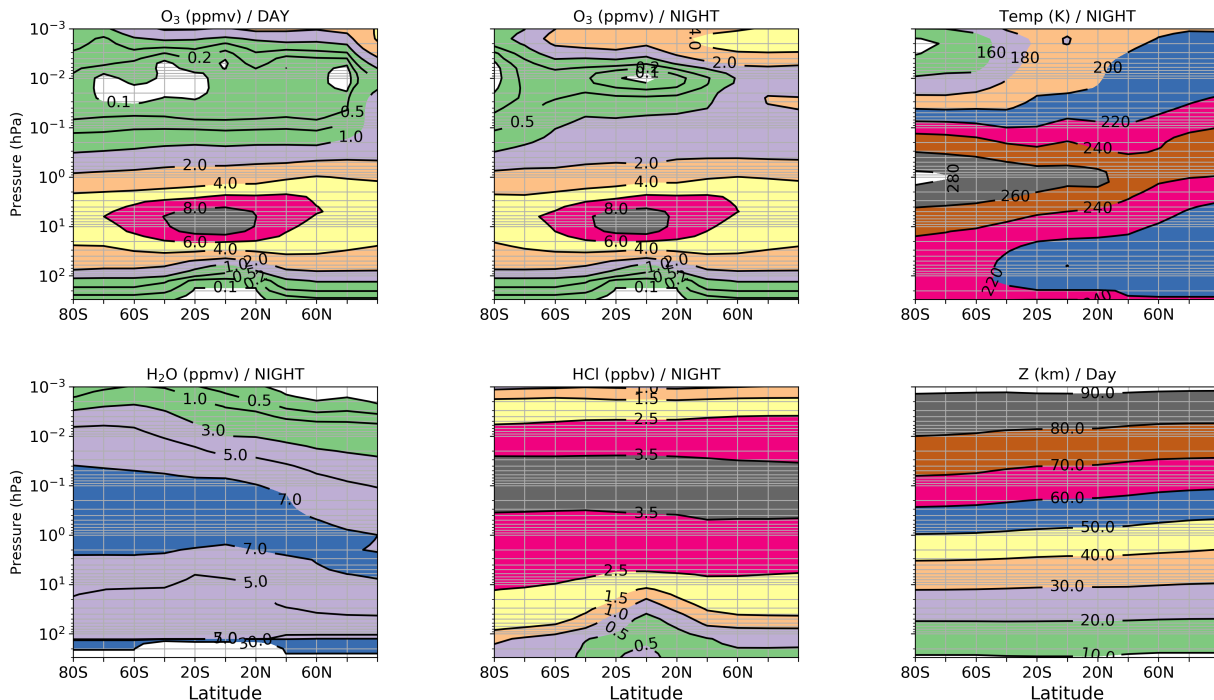
4.1 Reference atmosphere

Figure 5. Zonal mean distribution of the most relevant atmospheric parameters for the retrieval error assessment. The upper panels show the O_3 distributions on pressure levels for day and night labeled climatologies as well as the night temperature one. The lower panels show the night distributions for H_2O, HCl, and geopotential altitude. The white regions indicate values smaller than the color scales.

The measurement performances depend on the atmospheric state which depends on the latitude, season and local time. (For our calculations, we assume that the zonal variations of the mean atmospheric state are negligible.) The most relevant parameters to take into account are the profiles of O_3, H_2O, HCl, temperature and pressure (or geopotential height). A zonal-mean climatology of these parameters has been built, covering all latitudes divided into 11 bins (Fig. 5). These climatologies are based on Aura MLS observations (v3.3) performed between November 15 2009 and February 15 2010. This period has been chosen because of the strong contrast between the winter-pole and summer-pole conditions that provides large meridional variations of atmospheric states. Moreover, it was characterized by a stable northern polar vortex, which was not affected by any strong perturbation (Kuttippurath and Nikulin, 2012). MLS observes in the moving direction from a sun-synchronous platform. The orbit inclination is $98°$ from the Equatorial plane. Each latitude is observed at two different local-times, e.g. 1:45 and 13:45 LT at the Equator. These two LT are used to characterize the day- and night-time conditions though it is daytime (nighttime) for both LT over the southern (northern) boreal latitudes (Fig. 2). Bad data have been removed following the MLS

user's guide documentation (Livesey et al., 2011), except for the data flagged with negative errors that are biased toward the MLS retrieval a-priori. Using such data allows us to span the altitude coverage of the profiles up to 110 km with information suitable for this study. Other molecules are taken from the Whole Atmosphere Community Climate Model (WACCM) (Marsh et al., 2013) and extracted at the climatology latitudes and LT. For HOCl, HCN and CH3CN only tropical profiles are used. Because of their relatively weak signal, their variabilities do not impact the overall measurement performances and only typical abundances are needed to discuss the relevance of the measurement.
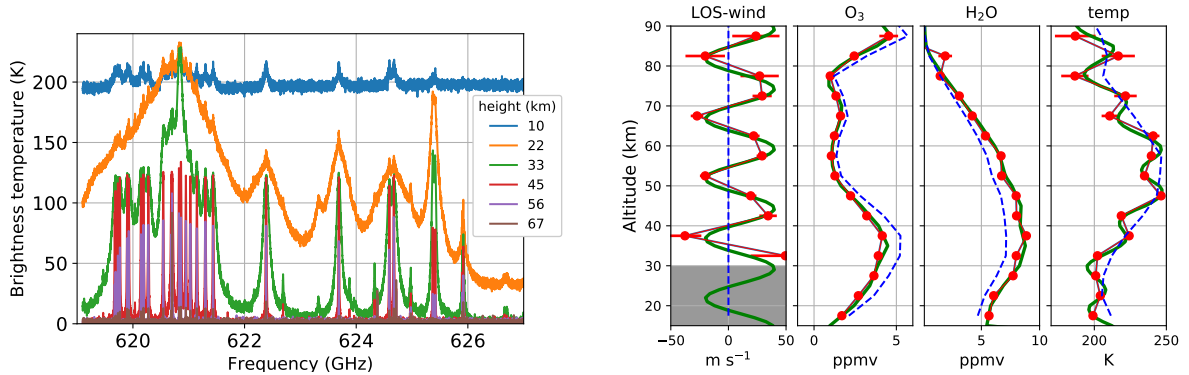
4.2 Retrieval Method

Figure 6. Left panel: Double sideband spectra with respect to the lower sideband frequency. Only a few spectra of the full vertical scan are shown (see legend). Right panel: Retrieved profiles with a vertical resolution of 5 km for nighttime arctic conditions. The blue-dashed lines are the a priori profiles (first guess), the green lines are the truth and the red line-circles are the retrieved values. The horizontal bars indicate the 1-σ errors due to instrument thermal noise.

The simulations are performed with the radiative transfer and retrieval codes used in the SMILES research processing chain (Baron et al., 2011) which has been validated with real observations (Kasai et al., 2013). The retrieved state $\hat{x}$ is a vector including all the unknown parameters of the forward model, namely the atmospheric vertical profiles, a radiance offset on each spectrum and a mean pointing angle offset of the whole scan. The atmospheric profiles are the volume mixing ratio (VMR) profiles of the chemical species, as well as those of temperature and LOS wind.

The retrieval altitudes range from 10 to 90 km, a range fully encompassed within the scan range (10–90 km). The grid resolution is 5 km corresponding to the effective vertical field-of-view of the instrument. Such a setting allows us to perform retrievals using a simple linear least-squares method with weak regularization. The retrieved vector is given by the equation:

$$\hat{x} = x_0 + (K^T S_{d,y}^{-1} K + U_x^{-1})^{-1} K^T S_{d,y}^{-1} (y - y_0), \tag{15}$$

where y is the measurement, x_0 is a first guess of the unknown parameters and y_0 is the associated simulated spectra, $K = \frac{\partial Tb}{\partial x}$ is the Jacobian matrix of the forward model (Eq. 1), $S_{d,y}$ is a diagonal matrix equal to the diagonal of S_y (Eq. 14), and U_x

is a diagonal matrix for stabilizing the matrix inversion. Its element square-roots correspond to very large standard deviations of $\boldsymbol{x}$, typically $> 10000\,\%$, $1000\,\text{K}$, $1000\,\text{m s}^{-1}$ for VMR, temperature and LOS wind, respectively. The regularization effects are negligible where the retrieval errors (null space and measurement errors) are much smaller than the $\boldsymbol{U}_x$ related STD. In other words, the averaging kernels are unity at altitudes where the measurement is relevant and the retrieval vertical resolution
5   is that of the retrieval altitude grid.

The retrieval precision is derived from the linear mapping of the measurement noise covariance onto the retrieved parameters space:

$$\epsilon_{x,\text{n}}^2 = \text{diag}(\boldsymbol{G}\boldsymbol{S}_y\boldsymbol{G}^T), \tag{16}$$

where $\epsilon_{x,\text{n}}$ is the standard deviation of $\hat{\boldsymbol{x}}$, $\boldsymbol{S}_y$ is the full measurement covariance matrix (Eq. 14) and $\boldsymbol{G} = (\boldsymbol{K}^T \boldsymbol{S}_{d,y}^{-1} \boldsymbol{K} +$
10   $\boldsymbol{U}_x^{-1})^{-1}\boldsymbol{K}^T \boldsymbol{S}_{d,y}^{-1}$.

Figure 6 (right panel) shows retrieved profiles of LOS-wind, O_3, H_2O and temperature using a simulated noisy measurement (Fig. 6, left panel). The measurement is computed using perturbed profiles from the climatology at 80°N/nighttime, hereafter named true profiles. The true profiles are defined with a vertical resolution of $0.5\,\text{km}$. The H_2O and HCl climatological profiles are multiplied by 1.2 and the O_3 one is multiplied by 0.8. An offset of $-5\,\text{K}$ ($10\,\text{m s}^{-1}$) and a 9 km-period oscillation with
15   an amplitude of 8 K (15 km, $30\,\text{m s}^{-1}$) are added on the temperature (wind) profile. A good agreement is found between the retrieved and true profiles. Below 40 km, the wind retrieval error strongly increases and we should consider that 30 km is the lower altitude for wind retrieval. The error increase is due to the pressure broadening of the lines that is about 30–40 MHz at 10 hPa. Other profiles are retrieved with low errors over most of the vertical range. A small oscillation is however seen on the H_2O profile that likely arises from the simple retrieval calculation (linearity and weak regularization). These results are
20   obtained with relatively large differences between the true and reference profiles and show that this retrieval setting can safely be used for the error analysis.

Systematic retrieval errors emerge from uncertainties on the instrument, calibration and forward model parameters, and LOS angles (Tab. 2). It is difficult at this stage of the mission definition to provide proper values for these uncertainties. The given values are relatively close to those expected but rounded in the way that it will be straight-forward to linearly scale the retrieval
25   errors according to any future better knowledge of the parameter uncertainties. One may notice that the uncertainty on the line broadening parameter (G_i) is likely underestimated and the actual values should be between 1–4 % depending on the line. On the other hand, the calibration parameters are likely overestimated. Anyway these errors induce relatively constant retrieval biases that could be mitigated with ad-hoc corrections if their properties are well understood, e.g., time scale and latitudinal variabilities (see for example the JEM/SMILES data analysis in Baron et al. (2013b)).
30   The 24-hours variability of the local oscillator frequency is between 2 and 10 kHz which straightly results to a LOS wind retrieval uncertainty of $1–5\,\text{m s}^{-1}$. The lower limit corresponds to the scientific requirement and the upper one is the worse acceptable case. Though it is a systematic error, it changes from one scan to another one with a time correlation that has to be determined before launch. The impacts on other retrieved parameters are negligible. Given the proposed design of the instrument (Murtagh, 2016), the 1-year frequency variability may be relatively large ($>0.5\,\text{MHz}$ or $250\,\text{m s}^{-1}$) and we should

Table 2. Systematic errors on observational and forward model parameters: calibration hot-load temperature (T_h, Eq. 12) and radiance linearity assumption (α, Eq. 11), sideband ratio (w_{lsb}, Eq. 1), local oscillator frequency (ν_{lo}, Eq. 1) over 24-hours and 1-year, antenna efficiency (η_a, Eq. 8), spectroscopic-line center frequency (F), pressure broadening (G) and strength (S), and LOS azimuth and elevation angles (θ, ϕ, Fig.4).

Calibration		Sideband ratio	Local oscillator		Ant. efficiency	Spectroscopy			LOS angles
ϵT_H	α	w_{lsb}	24 hours	1 year	η_a	F	G	S	θ, ϕ
1 %	0.5×10^{-5}	0.1%	$2 - 10 \ \mathrm{kHz}$	$> 0.5 \ \mathrm{MHz}$	$\sim \epsilon T_H$	10 kHz	1 %	1 %	0.5 mrad

consider that an absolute frequency knowledge, good enough for retrieving winds, may not be available. Frequency calibration will be performed using short-term wind retrieval bias estimates within 40–60 km where other systematic errors are small.

Retrieval errors from other parameters are investigated in Sect. 5.2 using a perturbation method:

$$\boldsymbol{\epsilon}_{x,\mathrm{p}} = \boldsymbol{G} \left(\boldsymbol{y}_{\mathrm{p}} - \boldsymbol{y}_0 \right), \tag{17}$$

where $\boldsymbol{\epsilon}_{x,\mathrm{p}}$ is the error induced by the parameter p and $\boldsymbol{y}_{\mathrm{p}}$ is the measurement assessed after changing the value of p according to its uncertainty. The spectroscopic errors are expressed for each molecule considering that the errors on the line parameters are mutually independent:

$$\boldsymbol{\epsilon}_{x,\mathrm{M}} = \sqrt{\sum_i \left(\boldsymbol{\epsilon}^2_{x,\mathrm{M},F_i} + \boldsymbol{\epsilon}^2_{x,\mathrm{M},G_i} + \boldsymbol{\epsilon}^2_{x,\mathrm{M},S_i} \right)}, \tag{18}$$

where $\boldsymbol{\epsilon}_{x,\mathrm{M}}$ denotes the total spectroscopic error due the molecule M, and F_i, G_i and S_i denote the center frequency, air-broadening parameter and line-strength of the line i.

The following errors will not be discussed. The errors on the LOS azimuth and elevation angles induces error smaller than $1 \ \mathrm{m\,s}^{-1}$ on the LOS wind retrievals. The mean elevation offset of the scan is retrieved with a precision better than $0.2 \ \mathrm{mrad}$. The retrieval error induced by the antenna efficiency is not discussed given that it has similar properties than that induced by the hot load emission error (Eq. 12).

5 Measurement performances

5.1 Retrieval precision

Results are discussed on pressure levels and the corresponding altitudes are shown in Figure 5. The precision ($1\text{-}\sigma$) is given for a single-scan and a vertical resolution of 5 km. It is possible to use the altitude information inscribes in the pressure broadened lineshape, for retrieving atmospheric profile with a better resolution but at the cost of the precision. Precision degradation can be afford for products retrieved from strong signals (e.g., O_3 or temperature) or for those whose the vertical resolution is more
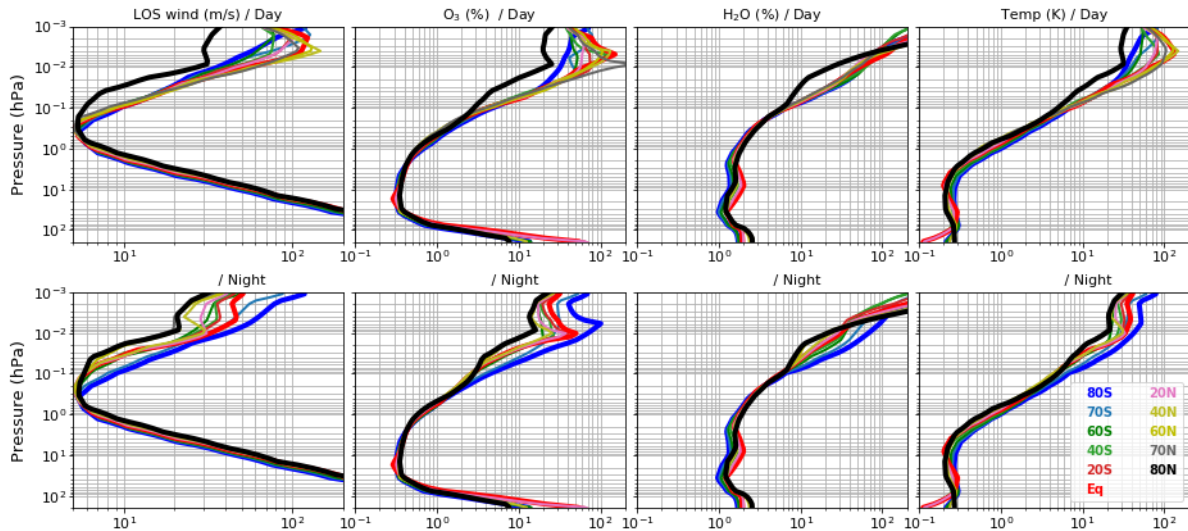
Figure 7. Single-scan retrieval precision (1-σ) for line-of-sight wind (left-most panels), O_3 (2nd column panels), H_2O (3rd column panels), and temperature (right-most panels). The line colors correspond to latitude bins (see legend) and thick lines are used for those corresponding to polar and equatorial regions. Errors are given for day- and nighttime labeled profiles. Note that southern (northern) polar profiles are actually both daytime (nighttime) ones.

scientifically relevant than the temporal or horizontal one (precision can be improved by averaging data). On the other hand, degrading the vertical resolution may be necessary for providing useful information on products derived from weak signals (e.g, HOCl). Later, using the results of this study and based on scientific requirements, the retrieval algorithm will be optimized for providing the best compromise between precision and resolution for each of the main products. Let's note that for all products

5 except for the LOS-wind, there are 2 quasi-simultaneous and quasi-coincident retrievals available from the two LOS (Fig. 2). They can be averaged for improving the precision by a factor $\sqrt{2}$.

5.1.1 O_3 retrieval

Figure 7 shows the retrieval precisions for temperature, LOS-wind and, O_3 and H_2O that have the strongest lines. A good precision is found for O_3 retrieval over the whole altitude range (200–0.001 hPa) because of the unusually large number of

10 lines compared to other MM/SMM missions. Between 100 and 0.2 hPa, the relative error is better than 2 % and does not vary significantly with latitudes and local times. A high precision <0.4 % is found between 50–2 hPa. There, the retrieval vertical resolution could be improved to 3–4 km with a precision of ≈ 1 % (not shown). In the upper part of the retrieval range, the relative precision strongly varies with latitudes and local-times. The errors are 30–50 % in nighttime and 40–100 % in daytime. The poorest relative precision is found near 0.01 hPa during daytime where most of O_3 is photo-dissociated (Fig. 5). Above,

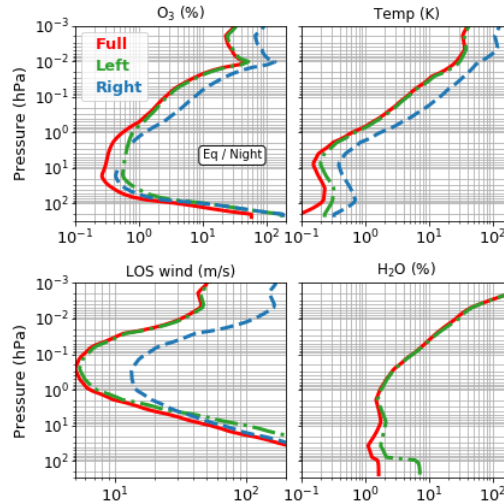15 the relative precision slightly improves due to the O_3 mesospheric secondary peak (Fig. 5).

16

Figure 8. Single-scan retrieval precision (1-σ) for O_3 and temperature (upper panels), and line-of-sight wind and H_2O (lower panels). Errors are calculated for a full band retrieval (red lines), the left half IF-band (10.075–14.075 GHz, blue lines) and the right half IF band (14.075–18.075 GHz, green lines). Results are shown for Equatorial nighttime conditions.

Figure 8 shows that above 1 hPa most of O_3 information is provided from the first half of the spectrum that contains the cluster of O_3 lines near 655 GHz (Fig. 3 and Fig. 6). Below this altitude, both sides of the spectrum contribute equally to the O_3 retrieval. The O_3-line cluster is the main source of information for the LOS wind and temperature retrievals above 4 hPa and 200 hPa, respectively (Fig. 8).

5 **5.1.2 Wind and temperature retrievals**

The performance of the LOS wind retrieval strongly depends on the O_3 abundance. With the current definition of the orbit (equator ascending node at 18:00 LT), most of the measurements are performed in nighttime (Fig. 2), which is a favorable case for measuring wind. The best performances are found over the northern polar region where the nighttime O_3 enhancement is the largest. There, the LOS-wind can be retrieved with a precision better than 10 m s^{-1} between 2 and 0.02 hPa (Fig. 7).

10 Comparable performances are found for nighttime equatorial and mid-latitude retrievals over a similar vertical range but with a slightly lower upper limit (0.03–0.04 hPa). In daytime, the uppermost altitude for obtaining similar precision dropped to 0.1 hPa over most of the latitudes. At 10 hPa, the error is 50–60 m s^{-1} and averaging 2 weeks of equatorial data in 10° latitude bin gives a precision of about 2 m s^{-1}. Since the precision is much poorer below this altitude, the 10 hPa level should be considered as the lowest altitude for obtaining useful wind information.

15 At 0.01 hPa, the nighttime LOS wind precision changes with latitudes from 20 m s^{-1} to 50 m s^{-1} (the southern polar profile is excluded) and from 40–60 m s^{-1} in daytime. At this altitude, the H_2O line at 620.7 GHz contributes significantly to the wind retrieval, especially during daytime. Over the polar regions, strong NO enhancements frequently occur in the middle

17

atmosphere due to energetic particle precipitation (EPP) (Randall et al., 2007; Pérot et al., 2014; Orsolini et al., 2017). During such events, the NO lines can be increased by more than a factor 10 that would improve the wind and temperature retrievals.

Temperature can be retrieved with a precision better than 1 K below 1 hPa. The retrieval vertical resolution can be improved to 3 km with a precision better than 1 K between 200 and 5 hPa (not shown). Above 0.2 hPa, the precision decreases to 10–30 K near 0.01 hPa in nighttime and to 30–80 K in daytime. During daytime most of the mesospheric information is provided by the strong H_2O line at 620.7 GHz.

5.1.3 H_2O and other molecules retrievals

The H_2O profile is retrieved from the line at 620.7 GHz and, below 100 hPa, from the continuum induced by far lines. The precision is better than 3 % (20 %) below 0.3 hPa (0.05 hPa). For altitudes above 0.1 hPa, the relative error increases and exhibits large latitudinal variations, e.g., 10–50 % at 0.2 hPa. The largest errors are found during daytime when the signal from O_3 is weak. Under such conditions, temperature is retrieved from the single H_2O line. The forward model inversion becomes ill-conditioned and both H_2O and temperature errors strongly increase. This issue is clearly illustrated with the much smaller H_2O daytime errors estimated without retrieving temperature compared to those with temperature retrieval (Fig. 9). Constraining the mesospheric temperature would significantly improve the mesospheric H_2O retrievals.

The retrieval precision for other molecules are shown in Fig. 9. First, we note that, except for O_3 and H_2O, all chemical species are retrieved from optically thin lines and the VMR error profiles have similar characteristics and are independent of the VMR values. The minimum VMR error is found near 10 hPa. Below, the errors increase due spectral line overlapping. The atmosphere becomes opaque near the tropopause. From the middle stratosphere to the mesosphere, the errors increase due to the decrease of atmospheric density (the error decreases only as $\approx$ pressure$^{-0.6}$ because the density decrease is partly compensated by the narrowing of the lines).

The best measurement performances with respect to the VMR are found for HCl, N_2O, HCN, CH3CN and HNO_3. Good information can also be inferred for the four most abundant O_3 isotopologues and from HDO. Important chemically active species such as ClO, NO, NO_2 or HO_2 can also be retrieved. If necessary the relative precision can be improved by averaging profiles or decreasing the retrieval vertical resolution. Deriving useful information for species such as BrO or HOCl will be challenging.

Chemically active species exhibit large variabilities. The photo-chemistry driven diurnal variation is the most common one. For instance, stratospheric ClO, NO and mesospheric HO_2 are more abundant in daytime but vanish in general during nighttime. Special events that occur more or less frequently can strongly increase the signal-to-noise ratio. For instance, ClO VMR frequently reaches 1.5 ppbv near 20 km during polar springtime due to the chlorine activation during the polar winter. The enhancement of SO_2 after strong volcanic eruption can also be measured (Pumphrey et al., 2015). EPP induced enhancement of NO_x and HO_x are an other example. During such events nighttime NO can reach levels of 10-100 ppbv between 10–0.1 hPa, levels much larger than the measurement single-scan precision (2–20 ppbv). EPP induced enhancements are not well represented in the models (Randall et al., 2007; Pérot et al., 2014; Orsolini et al., 2017) and SIW has a strong potential for providing key insights on their dynamical and chemical sources.
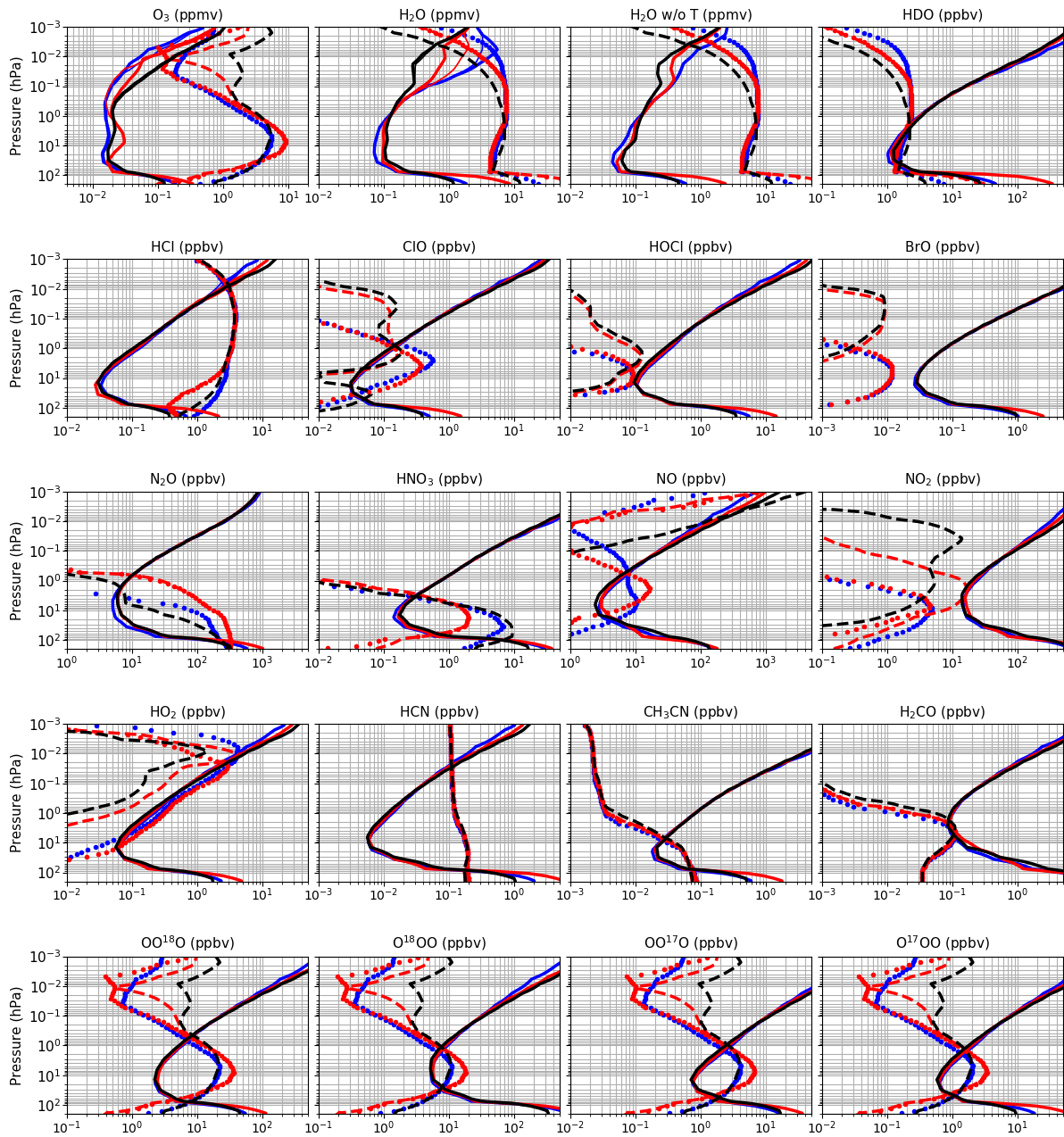
Figure 9. Retrieval single-scan precision (full lines), nighttime VMR (dashed lines) and daytime VMR (dotted lines) profiles. Profiles are shown at 80°S (blue line), Equator (red line) and 80°N (black line). The thick (thin) red full-lines are nighttime (daytime) conditions. The H_2O results without temperature retrieval are indicated with "w/o T".
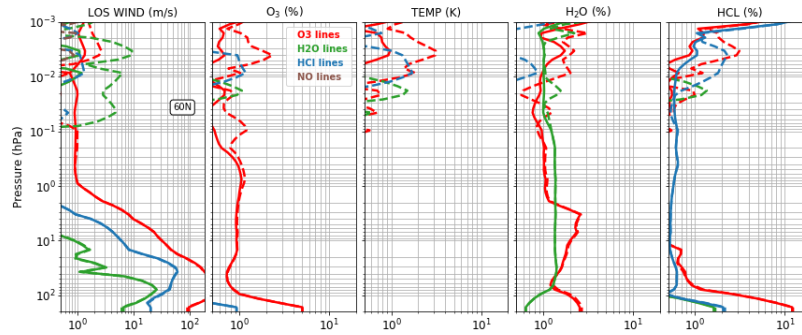
Figure 10. Spectroscopic induced errors on LOS wind, temperature, O_3, H_2O and HCl retrievals (see panel titles). The full-lines (dashed-lines) show the nigthtime (daytime) condition at 60N.
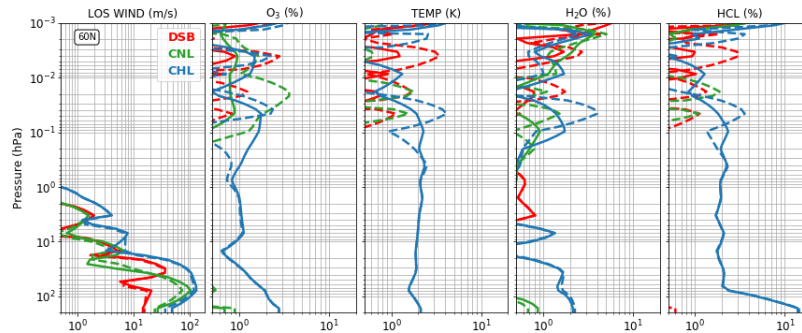

Figure 11. Same as Fig. 10 but for double-sideband ratio (DSB), radiometer nonlinearity (CNL) and calibration hot-load emission (CHL).The error assumptions are summarized in Tab. 2.

5.2 Systematic errors

The errors induced by the spectroscopic uncertainties on the most important lines have been estimated for the LOS-wind, temperature, O_3, H_2O and HCl retrievals. We consider the 50 most intense O_3 lines over the whole bandwidth, two HCl triplets (624.9 and 625.9 GHz), two NO triplets (651.4 and 651.7 GHz) and the 620.7 GHz H_2O line. Systematic errors induced by the double-sideband ratio (DSB), the calibration hot-load temperature and the radiometer non-linearity are also discussed for the same products.

5.2.1 Wind retrieval

Figure 10 clearly shows three altitude ranges for the wind retrieval errors induced by the spectroscopic parameters. Results are given for the latitude 60°N. Above 0.1 hPa, a daytime error of 3–5 $\mathrm{m\,s^{-1}}$ is induced by the frequency uncertainty on the H_2O line (Tab. A3). During nighttime, the signal is dominated by about 15 O_3-lines and a retrieval error of only 1 $\mathrm{m\,s^{-1}}$ is induced by their frequency uncertainty (Tab. A1 and A2). The same error of 1 $\mathrm{m\,s^{-1}}$ is found between 1 and 0.1 hPa both during day
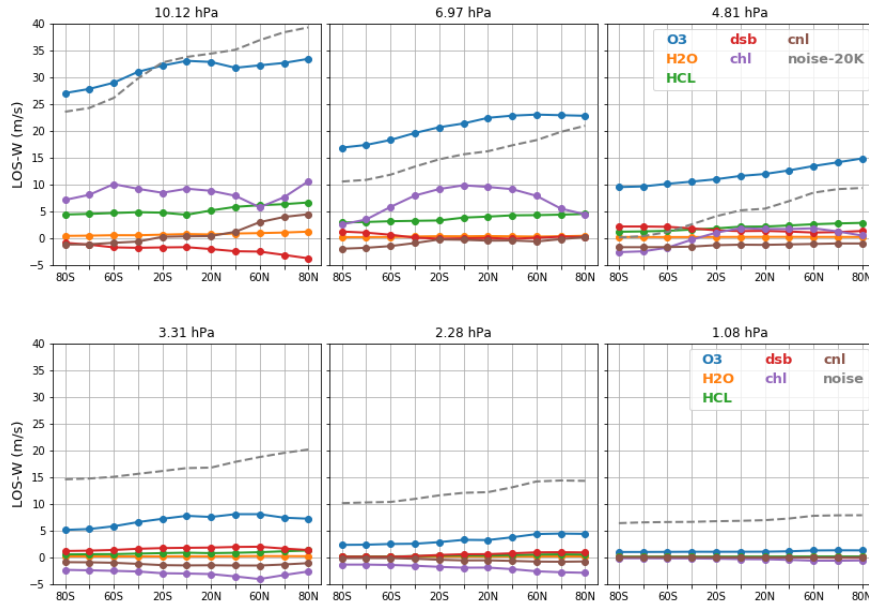
20

Figure 12. Line-of-sight wind retrieval biases with respect to latitudes near 10, 7 and 5 hPa (upper panels), and near 3, 2 and 1 hPa (lower panels). Biases are shown for the uncertainties on the spectroscopic parameters of O_3, HCl, and H_2O, the double-sideband ratio, the calibration hot load and the calibration non-linearity.

and night times. No impact of the NO lines has been found, even at higher latitudes, but this would not be the case for EPP enhanced profiles. Below 1 hPa, the lines broadened by the pressure overlap each other. Consequently the uncertainties on the air-broadening parameters and to a lesser extent, the line strength of the O_3 lines contribute to the retrieval error. The bias increases up to 20–30 $\mathrm{m\,s^{-1}}$ at 10 hPa.

5   Figure 11 shows the retrieval errors induced by the double-sideband ratio (DSB), the calibration hot-load temperature and the radiometer non-linearity. These parameters introduce errors on the wind retrieval only below 1 hPa. The uncertainty on the calibration hot-load temperature is the dominant retrieval error, reaching 5–8 $\mathrm{m\,s^{-1}}$ between 2–10 hPa. Overall, the O_3 lines parameters are the main source of error between 10–1 hPa for all latitudes (Fig. 12).

Methods for mitigating wind retrieval bias have to be developed taking into account SIW observation characteristics (see

10   Appendix A). For JEM/SMILES analysis, a retrieval bias of 20–40 $\mathrm{m\,s^{-1}}$ between 8–5 hPa was reduced to less than 4 $\mathrm{m\,s^{-1}}$ between 30S–50N by considering that the mean tropical flow is zonal (Baron et al., 2013b). Meteorological analyses and reanalysis at mid-latitudes can also be used for characterizing the retrieval biases below 5 hPa.

5.2.2 Temperature and VMR retrievals

The biases on O_3, HCl and temperature retrievals due to the spectroscopic parameters are small. They are lower than 1 % and 0.5 K between 100 and 0.02 hPa. Above 0.02 hPa, the biases increase but remain smaller than 5 % and 4 K. The errors are induced by the air-broadening and strength parameters of O_3 and H_2O lines. The strong impact of the H_2O line parameters onto the HCl retrieval reveals error amplifications due to the temperature retrieval. Using constraints on the temperature retrieval should allow us to reduce such effects.

The retrieval of H_2O above 0.2 hPa has a small bias <2 % that is induced by the uncertainties on the air-broadening and strength parameters of the 620.7 GHz H_2O line. Below this altitude, the retrieval error reaches 5 % mainly due to the air-broadening parameters of the overlapping O_3 lines at 620.69 and 623.669 GHz (Tab. A1). Below 100 hPa, the H_2O lines outside the band are the main signal for the retrieval (not shown), and the 620.7 GHz H_2O line weight in the retrieval is small.

The DSB and calibration parameters induced errors on O_3, HCl and temperature retrievals are small below 0.1 hPa, i.e., lower than 3 % and 2 K (Fig. 11). The calibration hot-load temperature and the radiometer non-linearity dominate the temperature retrieval error. The VMR and temperature retrievals are also sensitive to the DSB uncertainties and radiometer non-linearity above 0.1 hPa, especially in daytime. The daytime errors are likely increased by the temperature retrieval.

6 Conclusions

A simulation study has been conducted to support the mission definition of SIW and to assess the measurement performances. This small mission will be launched near 2022 for monitoring the middle-atmosphere (10–90 km) using the thermal emission lines near 640 GHz of a large number of chemical species. This analysis focuses on the main outcomes, namely LOS wind, temperature, O_3 and more than a dozen of other chemical species. The error assessment is performed taking into account the day-night and latitudinal atmospheric variabilities.

The unusually large number of strong O_3 lines at 653–657 GHz allows us to measure the 2-d horizontal wind between 10 and 0.001 hPa and temperature between 100 and 0.1 hPa as well as providing a high-sensitivity to O_3 between 100–0.001 hPa. LOS wind is an original outcome for such a mission. It demands a special observation setting involving 2 antennas in order to retrieve two perpendicular components of the wind vector. Each component can be measured between 2 and 0.03 hPa with a precision better than $10 \, \mathrm{m\,s^{-1}}$ and vertical resolution of 5 km. Other spaceborne instruments have poor sensitivity in this altitude range. A sunsynchronous polar orbit allowing us to perform night-time measurements is currently considered. Such conditions are the most favorable for mesospheric wind, temperature and ozone measurements but not for active chemical species such as stratospheric ClO or strato-mesospheric HO_2 that generally vanish during nighttime.

The impact of systematic errors induced by the spectroscopic parameters and, by the instrument and calibration parameters are discussed. This work highlights the need for a good characterization of the spectroscopic parameters (air-broadening, strength, and center frequency and pressure shift) of key O_3, H_2O and NO lines. Even so, a large wind measurement bias may occur between 10 and 2 hPa mainly due to errors on O_3 line air-broadening parameters. Hence ad-hoc methods for reducing retrieval biases must be studied. These methods can be used to calibrate the LO frequency long-term trend that may arise with

the proposed hardware. However, improvements of the instrument design for following the LO frequency with a precision better than 2 kHz, are still being investigated.

SIW shows a strong potential for the study of various scientific issues. It can provide for the first time global information on the horizontal wind between 30–90 km that can be used to validate chemical and climate models. It has the potential for con-
5   tributing to the characterization of long trend series of temperature, O_3, H_2O and HCl, that are important for climate studies and for monitoring the chemical composition of the mid-atmosphere. The mission can provide data to study the dynamics of the middle atmosphere. Based on SIW observations, specific studies on key dynamical processes, such as the quasi-biennial oscillation, the semi-annual oscillation or sudden stratospheric events for example, could be carried out. A better understanding of these phenomena, in addition to global mid-atmospheric wind measurements, would significantly improve our knowledge
10 of the climate system. Not discussed in this paper is also the capability of SIW for measuring ice water content in the tropical upper-troposphere (Eriksson et al., 2014). Observing the same air-mass from two perpendicular directions could provide interesting information considering the high spatial inhomogeneities of cloudy scenes.

Optimization of the calibration procedure will be studied in order to improve the measurement precision. Here we have assumed an equal observation time for the cold-sky and atmosphere measurements. Changing the time sharing in favor of
15 atmospheric observations could improve the measurement sensitivity by more than 20 %. The retrievals could also be improved in the mesosphere by increasing the frequency resolution to 0.5 MHz at the intermediate frequency range between 17.2 and 17.4 GHz that contains the strong H2O line (620.701 GHz) and the two strongest O3 lines (620.825 and 655.289 GHz). Implementing such a setting is under investigation.

The InnoSat platform offers a quick opportunity to fly SIW. This is important since the current SMM limb missions have
20 already exceeded by far their lifetime expectations and they risk to stop soon. However such a platform strongly limits the design of a SMM instrument and its performances. A larger antenna would improve the vertical resolution and an additional receiver with a narrow bandwidth measuring an oxygen or a strong water vapor line would significantly improve the wind and temperature retrievals in the mesosphere. Such improvements are studied for the much larger SMILES-2 mission (Ochiai et al., 2017) presented in the introduction section and which also includes the same spectral window as SIW. However this mission
25 can not be launched before 2025 if selected.

Appendix A: LOS and horizontal winds

The retrieval of two line-of-sight winds over the same region allows us to compute the meridional (V) and zonal (U) components of the horizontal wind vector. Applying Eq. (6) to the forward and aftward viewing antenna, the two retrieved LOS
30 winds are:

$$
\begin{aligned}
V_{\mathrm{los,fwd}} &= U\sin(\phi_n) + V\cos(\phi_n) \\
V_{\mathrm{los,aft}} &= U\sin(\phi_n + \delta) + V\cos(\phi_n + \delta)
\end{aligned}
\tag{A1}
$$

where ϕ_n is the angle of the forward-looking line-of-sight with respect to the north direction and δ is the angle between the two lines of sight. It is straight forward to show that

$$U = \frac{1}{\sin(\delta)} \left(V_{\text{los,aft}} \cos(\phi_n) - V_{\text{los,fwd}} \cos(\phi_n + \delta) \right) \tag{A2}$$

$$V = \frac{1}{\sin(\delta)} \left(V_{\text{los,fwd}} \sin(\phi_n + \delta) - V_{\text{los,aft}} \sin(\phi_n) \right)$$

5   and the random errors on U and V are:

$$\epsilon_U = \frac{\epsilon_{\text{los}}}{\sin(\delta)} \sqrt{\cos(\phi_n + \delta)^2 + \cos(\phi_n)^2}$$

$$\epsilon_V = \frac{\epsilon_{\text{los}}}{\sin(\delta)} \sqrt{\sin(\phi_n + \delta)^2 + \sin(\phi_n)^2} \tag{A3}$$

where ϵ_{los} is line-of-sight wind retrieval error.

For $\delta = 90°$, we have:

10   $$U = \left(V_{\text{los,aft}} \cos(\phi_n) + V_{\text{los,fwd}} \sin(\phi_n) \right)$$

$$V = \left(V_{\text{los,fwd}} \cos(\phi_n) - V_{\text{losaft}} \sin(\phi_n) \right).$$

The random error on each wind component becomes $\epsilon_U = \epsilon_V = \epsilon_{\text{los}}$. This configuration is that for which $\epsilon_U^2 + \epsilon_V^2 = 2 \left(\epsilon_{\text{los}} / \sin(\delta) \right)^2$ is minimum. A systematic error e_{los} on the LOS wind retrievals propagates to the U and V components as follows:

1. The systematic error on the zonal wind estimate is $e_u = e_{\text{los}} \left(\cos(\phi_n) + \sin(\phi_n) \right)$

15   2. The systematic error on the meridional wind estimate is $e_v = e_{\text{los}} \left(\cos(\phi_n) - \sin(\phi_n) \right)$.

We assume that e_{los} does not depends on the LOS orientation which is a valid assumption for the errors investigated in this paper (LO frequency, calibration, spectroscopy). We should note that $e_v = 0$ for $\phi_n = 45$ ° or 225 ° which occurs at latitudes between 30°N–50°N on the ascending branch of the orbit and between 10°N–30°N on the descending branch. The cases $e_u = 0$ occur for the measurements from the orbit positions with the lowest and highest latitudes.

20   At the equator, the bias on the meridional wind is partly canceled out. For instance, an error $e_{\text{los}} = 1.0 \text{ m s}^{-1}$ induces an error $e_v = 0.2 \text{ m s}^{-1}$. Hence, using the tropical zonal-wind to characterize the measurement bias as it was done in the JEM/SMILES analysis may not be a satisfactory method for SIW. On the other hand, $e_{\text{los}} = 1.0 \text{ m s}^{-1}$ leads to an error $e_u = 1.4 \text{ m s}^{-1}$ on the zonal component with an opposite sign on the ascending and descending orbit branches. The sign difference may provide us with a way to characterize LOS wind retrieval systematic errors.

25   **Appendix B: Spectroscopic lines**

The following tables show the most relevant spectroscopic lines for the retrievals of the LOS wind, O_3, Temperature, H_2O and HCl. The relative retrieval impact of each parameter is defined as:

$$\varrho_{x,\mathrm{M},p_i} = \frac{\epsilon_{x,\mathrm{M},p_i}}{max(\{\epsilon_{x,\mathrm{M},p_i}\}_{p,i})} \quad \text{with } p_i = F_i,\ G_i \text{ or } S_i, \tag{B1}$$

where M denotes the chemical species, $\epsilon_{x,\mathrm{M},p_i}$ is the error induced by the parameter p of the line i (Eq. 18), and $\{\epsilon_{x,\mathrm{M},p_i}\}_{p,i}$ is the set of errors induced by all the parameters of all the lines of the species M.

Table A1. Relative impact of O_3 line parameters on temperature, O_3, H_2O and LOS wind retrievals. For a retrieved product, the impact is defined as error to the maximum error ratio (see text). Results are given for 10, 1 and 0.1 hPa levels (Equatorial night-time conditions). Only parameters having an impact larger than 0.5 at any of the considered altitudes are shown. The parameters are the center frequency (S), the air-broadening parameter (G) and the line strength (S). The line is characterized by its frequency (MHz).

Parameter	LOS wind			O3			Temperature			H2O			HCl		
					Lower sideband										
620687-F	-	-	0.6	-	-	-	-	-	-	-	-	-	-	-	-
-G	-	-0.5	-	-	-	-	-	-	-	0.8	0.5	-	-	-	-
-S	-	**-1.0**	-	-	-	-	-	-	-0.5	**1.0**	0.7	-	-	-	-
620825-F	-	0.6	**1.0**	-	-	-	-	-	-	-	-	-	-	-	-
-G	0.8	-	-	-	-	-	-	0.9	-	0.7	-	-	-	-	-
-S	0.7	-	-	-	-	-	-	**1.0**	0.8	0.6	-	-	-	-	-
623688-F	-	0.8	0.7	-	-	-	-	-	-	-	-	-	-	-	-
-G	-	-	-	-	-	-	0.8	-	-	-0.7	-0.5	-	-	-	-
-S	-	-	-	-	-	-	1.0	-	-	-0.8	-0.5	-	-	-	-
625370-F	-	0.7	-	-	-	-	-	-	-	-	-	-	-	-	-
-G	-1.0	-	-	-	-	-	-	-	-	-	-	-	-	-	-
-S	-	-	-	**1.0**	**1.0**	**1.0**	**-1.0**	-	0.5	-	**1.0**	**1.0**	-	**1.0**	**1.0**
					Upper sideband										
650732-F	-	0.7	-	-	-	-	-	-	-	-	-	-	-	-	-
-G	**-1.0**	-	-	-	-	-	-	-	-	-	-	-	-	-	-
-S	-0.5	-	-	0.9	0.9	0.9	-0.9	-	-	-	0.9	0.9	-	1.0	0.9
651475-F	-	0.7	1.0	-	-	-	-	-	-	-	-	-	-	-	-
-G	-0.5	-	-	-	-	-	-	-	-	-	-	-	1.0	-	-
-S	-0.6	-	-	-	-	-	-	-	-	-0.5	-	-	**1.0**	-	-
651556-F	-	0.9	0.5	-	-	-	-	-	-	-	-	-	-	-	-
-S	-	-	-	-	-	-	-	-	-0.9	-	-	-	-	-	-
653763-F	-	0.7	0.9	-	-	-	-	-	-	-	-	-	-	-	-
-G	-	-	-	-	-	-	-	-	-	-	-	-	-0.6	-	-
-S	-	-	-	-	-	-	-	-	-	-	-	-	-0.6	-	-

Table A2. Continuation of Tab. A1.

Parameter	LOS wind			O3			Temperature			H2O			HCl		
654713-F	-	0.7	0.9	-	-	-	-	-	-	-	-	-	-	-	-
-S	-0.5	-	-	-	-	-	-	-	-	-	-	-	-	-	-
654851-F	-	0.7	0.9	-	-	-	-	-	-	-	-	-	-	-	-
655004-F	-	0.7	0.8	-	-	-	-	-	-	-	-	-	-	-	-
655121-F	-	0.7	0.8	-	-	-	-	-	-	-	-	-	-	-	-
655202-F	-	0.7	0.9	-	-	-	-	-	-	-	-	-	-	-	-
655289-F	-	0.6	1.0	-	-	-	-	-	-	-	-	-	-	-	-
-G	-	-	-	-	-	-	-	0.5	-	-	-	-	-	-	-
-S	-	-	-	-	-	-	-	0.6	0.8	-	-	-	-	-	-
655607-F	-	0.7	0.9	-	-	-	-	-	-	-	-	-	-	-	-
-S	-	-	-	-	-	-	-	-	-	-	0.5	-	-	-	-
655873-F	-	0.7	0.9	-	-	-	-	-	-	-	-	-	-	-	-
655960-F	-	0.7	0.9	-	-	-	-	-	-	-	-	-	-	-	-
656005-F	-	0.8	0.8	-	-	-	-	-	-	-	-	-	-	-	-
-S	-	-	-	-	-	-	-	-	0.5	-	-	-	-	-	-
656224-F	-	0.7	0.8	-	-	-	-	-	-	-	-	-	-	-	-
656251-F	-	0.7	0.7	-	-	-	-	-	-	-	-	-	-	-	-
656383-F	-	0.8	0.6	-	-	-	-	-	-	-	-	-	-	-	-
-S	-	-	-	-	-	-	-	-	-0.6	-	-	-	-	-	-
656419-F	-	0.8	0.5	-	-	-	-	-	-	-	-	-	-	-	-
-S	-	-	-	-	-	-	-	-	-0.9	-	-	-	-	-	-
656461-F	-	0.7	-	-	-	-	-	-	-	-	-	-	-	-	-
-S	-	-	-	-	-	-	-	-	**-1.0**	-	-	-	-	-	-
656476-F	-	0.6	-	-	-	-	-	-	-	-	-	-	-	-	-
-S	-	-	-	-	-	-	-	-	-0.7	-	-	-	-	-	-

Table A3. Same as Tab. A1 but for the H_2O line parameters

Parameter	LOS wind			O3			Temperature			H2O			HCl		
620701-F	-	**1.0**	**1.0**	-	**-1.0**	-	-	-	-	-	-	-	-	0.5	-
-G	**1.0**	**-1.0**	-	0.9	0.8	**1.0**	0.6	-	**1.0**	0.9	0.9	0.7	0.7	-	**1.0**
-S	-	-	-	**1.0**	0.7	-	**1.0**	**1.0**	-	**1.0**	**1.0**	**1.0**	**1.0**	**1.0**	-
622482-G	-	-	-	-	-0.5	-	-	-	-	-	-	-	-	-	-
-S	-0.8	-	-	-	0.7	-	-	-	-	-	-	-	-	-	-

Table A4. Same as Tab. A1 but for the HCl line parameters.

Parameter	LOS wind			O3			Temperature			H2O			HCl		
624964-S	-0.6	-	-	-	-	-	-0.6	0.5	-	-	-	-	-	-	-
624977-G	-	-	-	-	-	-	0.6	-	-	-	-	-	-	-	-
-S	-	-	-	-	-	-	-1.0	0.5	-	-	-	-	-	-	-
625901-F	-	0.6	0.6	-	-	-	-	-	-	-	-	-	-	-	-
-G	0.9	-	-	-0.7	-0.7	-0.6	-0.6	-0.9	-	-	-0.6	-0.6	-	-	-
-S	**-1.0**	-	-	-	-	-	**1.0**	-	0.5	-	-	-	0.7	0.5	0.6
625918-F	-	**1.0**	**1.0**	-	-	-	-	-	0.5	-	-	-	-	-	-
-G	-	-	-	**-1.0**	**-1.0**	**-1.0**	-	**-1.0**	**1.0**	**-1.0**	**-1.0**	**-1.0**	-	-0.5	-
-S	1.0	-	-	-	-	-	0.6	-1.0	0.6	0.7	-	-	**1.0**	**1.0**	**1.0**
625931-G	-0.6	-	-	-	-	-	-	-0.5	-	-	-	-	-	-	-
-S	**1.0**	-	-	-	-	-	-	-	-0.7	-	-	-	-	-	-

References

Baldwin, M., Thompson, D. W. J., Shuckburgh, E. F., Norton, W. A., and Gillett, N. P.: Weather from the Stratosphere?, Science, 301, 317–318, 2003.

Baldwin, M. P., Gillett, N. P., Forster, P., Gerber, E. P., Hegglin, M. I., Karpechko, A. Y., Kim, J., Kushner, P. J., Morgenstern, O. H., and
5 Reichler, T.: Effects of the Stratosphere on the Troposphere, chap. 10, WMO/ICSU/IOC World Climate Research Programme, 2010.

Baron, P., Urban, J., Sagawa, H., Möller, J., Murtagh, D. P., Mendrok, J., Dupuy, E., Sato, T. O., Ochiai, S., Suzuki, K., Manabe, T., Nishibori, T., Kikuchi, K., Sato, R., Takayanagi, M., Murayama, Y., Shiotani, M., and Kasai, Y.: The Level 2 research product algorithms for the Superconducting Submillimeter-Wave Limb-Emission Sounder (SMILES), Atmos. Meas. Techn., 4, 2105–2124, doi:10.5194/amt-4-2105-2011, http://www.atmos-meas-tech.net/4/2105/2011/, 2011.

10 Baron, P., Murtagh, D. P., Urban, J., Sagawa, H., Eriksson, P., and Ochiai, S.: Definition of an uncooled Sub-Millimeter/THz Limb sounder for measuring middle atmospheric winds, ESA Living Planet Symposium, 9-13 September, Edinburgh (UK), pp. 1–8, 2013a.

Baron, P., Murtagh, D. P., Urban, J., Sagawa, H., Ochiai, S., Kasai, Y., Kikuchi, K., Khosrawi, F., Körnich, H., Mizobuchi, S., Sagi, K., and Yasui, M.: Observation of horizontal winds in the middle-atmosphere between 30S and 55N during the northern winter 2009–2010, Atmospheric Chemistry and Physics, 13, 6049–6064, doi:10.5194/acp-13-6049-2013, 2013b.

15 Baumgarten, G.: Doppler Rayleigh/Mie/Raman lidar for wind and temperature measurements in the middle atmosphere up to 80 km, Atmospheric Measurement Techniques, 3, 1509–1518, doi:10.5194/amt-3-1509-2010, https://www.atmos-meas-tech.net/3/1509/2010/, 2010.

Blanc, E., Ceranna, L., Hauchecorne, A., Charlton-Perez, A., Marchetti, E., Evers, L. G., Kvaerna, T., Lastovicka, J., Eliasson, L., Crosby, N. B., Blanc-Benon, P., Le Pichon, A., Brachet, N., Pilger, C., Keckhut, P., Assink, J. D., Smets, P. S. M., Lee, C. F., Kero, J., Sindelarova, T., Kämpfer, N., Rüfenacht, R., Farges, T., Millet, C., Näsholm, S. P., Gibbons, S. J., Espy, P. J., Hibbins, R. E., Heinrich, P., Ripepe, M.,
20 Khaykin, S., Mze, N., and Chum, J.: Toward an Improved Representation of Middle Atmospheric Dynamics Thanks to the ARISE Project, Surveys in Geophysics, 39, 171–225, doi:10.1007/s10712-017-9444-0, https://doi.org/10.1007/s10712-017-9444-0, 2018.

Christensen, O. M., Eriksson, P., Urban, J., Murtagh, D., Hultgren, K., and Gumbel, J.: Tomographic retrieval of water vapour and temperature around polar mesospheric clouds using Odin-SMR, Atmospheric Measurement Techniques, 8, 1981–1999, doi:10.5194/amt-8-1981-2015, http://www.atmos-meas-tech.net/8/1981/2015/, 2015.

25 Duruisseau, F., Huret, N., Andral, A., and Camy-Peyret, C.: Assessment of the ERA-Interim Winds Using High-Altitude Stratospheric Balloons, Journal of the Atmospheric Sciences, 74, 2065–2080, doi:10.1175/JAS-D-16-0137.1, https://doi.org/10.1175/JAS-D-16-0137.1, 2017.

Eriksson, P., Rydberg, B., Sagawa, H., Johnston, M. S., and Kasai, Y.: Overview and sample applications of SMILES and Odin-SMR retrievals of upper tropospheric humidity and cloud ice mass, Atmospheric Chemistry and Physics, 14, 12 613–12 629, doi:10.5194/acp-
30 14-12613-2014, https://www.atmos-chem-phys.net/14/12613/2014/, 2014.

Gerber, E. P., Butler, A., Calvo, N., Charlton-Perez, A., Giorgetta, M., Manzini, E., Perlwitz, J., Polvani, L. M., Sassi, F., Scaife, A. A., Shaw, T. A., Son, S.-W., and Watanabe, S.: Assessing and Understanding the Impact of Stratospheric Dynamics and Variability on the Earth System, Bull. Amer. Meteor. Soc., 93, 845–859, doi:10.1175/bams-d-11-00145.1, https://doi.org/10.1175/BAMS-D-11-00145.1, 2012.

Hegglin, M. I. and Tegtmeier, S.: The SPARC Data Initiative: Assessment of stratospheric trace gas and aerosol climatologies from satellite
35 limb sounders., SPARC Report No. 8, WCRP-5/2017, www.sparc-climate.org/publications/sparc-reports/, 2017.

Hoppel, K. W., Baker, N. L., Coy, L., Eckermann, S. D., McCormack, J. P., Nedoluha, G. E., and Siskind, D. E.: Assimilation of stratospheric and mesospheric temperatures from MLS and SABER into a global NWP model, Atmospheric Chemistry and Physics, 8, 6103–6116, doi:10.5194/acp-8-6103-2008, http://www.atmos-chem-phys.net/8/6103/2008/, 2008.

Ishii, S., Baron, P., Aoki, M., Mizutani, K., Yasui, M., Ochiai, S., Sato, A., Satoh, Y., Kubota, T., Sakaizawa, D., Oki, R., Okamoto, K., Ishibashi, T., Tanaka, T. Y., Sekiyama, T. T., Maki, T., Yamashita, K., Nishizawa, T., Satoh, M., and Iwasaki, T.: Feasibility Study for Future Space-Borne Coherent Doppler Wind Lidar, Part 1: Instrumental Overview for Global Wind Profile Observation, Journal of the Meteorological Society of Japan. Ser. II, 95, 301–317, doi:10.2151/jmsj.2017-017, 2017.

Jarnot, R. F., Perun, V. S., and Schwartz, M. J.: Radiometric and spectral performance and calibration of the GHz bands of EOS MLS, IEEE Transactions on Geoscience and Remote Sensing, 44, 1131–1143, 2006.

Kasai, Y., Sagawa, H., Kreyling, D., Dupuy, E., Baron, P., Mendrok, J., Suzuki, K., Sato, T. O., Nishibori, T., Mizobuchi, S., Kikuchi, K., Manabe, T., Ozeki, H., Sugita, T., Fujiwara, M., Irimajiri, Y., Walker, K. A., Bernath, P. F., Boone, C., Stiller, G., von Clarmann, T., Orphal, J., Urban, J., Murtagh, D., Llewellyn, E. J., Degenstein, D., Bourassa, A. E., Lloyd, N. D., Froidevaux, L., Birk, M., Wagner, G., Schreier, F., Xu, J., Vogt, P., Trautmann, T., and Yasui, M.: Validation of stratospheric and mesospheric ozone observed by SMILES from International Space Station, Atmospheric Measurement Techniques, 6, 2311–2338, doi:10.5194/amt-6-2311-2013, https://www.atmos-meas-tech.net/6/2311/2013/, 2013.

Kawatani, Y., Hamilton, K., Miyazaki, K., Fujiwara, M., and Anstey, J. A.: Representation of the tropical stratospheric zonal wind in global atmospheric reanalyses, Atmospheric Chemistry and Physics, 16, 6681–6699, doi:10.5194/acp-16-6681-2016, https://www.atmos-chem-phys.net/16/6681/2016/, 2016.

Khosravi, M., Baron, P., Urban, J., Froidevaux, L., Jonsson, A. I., Kasai, Y., Kuribayashi, K., Mitsuda, C., Murtagh, D. P., Sagawa, H., Santee, M. L., Sato, T. O., Shiotani, M., Suzuki, M., von Clarmann, T., Walker, K. A., and Wang, S.: Diurnal variation of stratospheric and lower mesospheric $HOCl$, ClO and HO_2 at the equator: comparison of 1-D model calculations with measurements by satellite instruments, Atmospheric Chemistry and Physics, 13, 7587–7606, doi:10.5194/acp-13-7587-2013, https://www.atmos-chem-phys.net/13/7587/2013/, 2013.

Kikuchi, K., Nishibori, T., Ochiai, S., Ozeki, H., Irimajiri, Y., Kasai, Y., Koike, M., Manabe, T., Mizukoshi, K., Murayama, Y., Nagahama, T., Sano, T., Sato, R., Seta, M., Takahashi, C., Takayanagi, M., Masuko, H., Inatani, J., Suzuki, M., and Shiotani, M.: Overview and early results of the Superconducting Submillimeter-Wave Limb-Emission Sounder (SMILES), J. Geophys. Res., 115, D23 306, http://dx.doi.org/10.1029/2010JD014379, 2010.

Kursinski, E. R., Hajj, G. A., Schofield, J. T., Linfield, R. P., and Hardy, K. R.: Observing Earth's atmosphere with radio occultation measurements using the Global Positioning System, Journal of Geophysical Research: Atmospheres, 102, 23 429–23 465, doi:10.1029/97JD01569, http://dx.doi.org/10.1029/97JD01569, 1997.

Kuttippurath, J. and Nikulin, G.: A comparative study of the major sudden stratospheric warmings in the Arctic winters 2003/2004–2009/2010, Atmospheric Chemistry and Physics, 12, 8115–8129, doi:10.5194/acp-12-8115-2012, https://www.atmos-chem-phys.net/12/8115/2012/, 2012.

Le Pichon, A., Assink, J. D., Heinrich, P., Blanc, E., Charlton-Perez, A., Lee, C. F., Keckhut, P., Hauchecorne, A., Rüfenacht, R., Kämpfer, N., Drob, D. P., Smets, P. S. M., Evers, L. G., Ceranna, L., Pilger, C., Ross, O., and Claud, C.: Comparison of co-located independent ground-based middle atmospheric wind and temperature measurements with numerical weather prediction models, Journal of Geophysical Research: Atmospheres, 120, 8318–8331, doi:10.1002/2015JD023273, http://dx.doi.org/10.1002/2015JD023273, 2015JD023273, 2015.

Limpasuvan, V., Richter, J. H., Orsolini, Y. J., Stordal, F., and Kvissel, O.-K.: The roles of planetary and gravity waves during a major stratospheric sudden warming as characterized in WACCM, Journal of Atmospheric and Solar-Terrestrial Physics, 78-79, 84 – 98, doi:https://doi.org/10.1016/j.jastp.2011.03.004, http://www.sciencedirect.com/science/article/pii/S1364682611000733, structure and Dynamics of Mesosphere and Lower Thermosphere, 2012.

5 Lindberg, R.: Call for Proposals for a Scientific Swedish Satellite based on the InnoSat Platform, http://www.rymdstyrelsen.se/en/Home/Home/, 2016.

Livesey, N. J. and Santee, M. L.: Prospects for future spaceborne measurements of interest to the SPARC DA Community and how to improve those prospects, in: S-RIP 2017 and 13th SPARC-DA Workshop, https://events.oma.be/indico/event/18/material/slides/16.pdf, 2017.

Livesey, N. J., Snyder, W. V., Read, W. G., and Wagner, P. A.: Retrieval algorithms for the EOS Microwave limb sounder (MLS), IEEE

10 Transactions on Geoscience and Remote Sensing, 44, 1144–1155, doi:10.1109/TGRS.2006.872327, 2006.

Livesey, N. J., Read, W. G., Froidevaux, L., Lambert, A., Manney, G. L., Pumphrey, H. C., Santee, M. L., Schwartz, M. J., Wang, S., Cofield, R. E., Cuddy, D. T., Fuller, R. A., Jarnot, R. F., Jiang, J. H., Knosp, B. W., Stek, P. C., Wagner, P. A., and Wu., D. L.: EOS MLS Level 2 Version 3.3 Quality Document, Tech. rep., Jet Propulsion Laboratory, California Institute of Technology, Pasadena, California, 91109-8099, http://mls.jpl.nasa.gov/data/datadocs.php, 2011.

15 Marsh, D. R., Mills, M. J., Kinnison, D. E., Lamarque, J.-F., Calvo, N., and Polvani, L. M.: Climate Change from 1850 to 2005 Simulated in CESM1(WACCM), Journal of Climate, 26, 7372–7391, doi:10.1175/JCLI-D-12-00558.1, 2013.

Millán, L., Wang, S., Livesey, N., Kinnison, D., Sagawa, H., and Kasai, Y.: Stratospheric and mesospheric HO_2 observations from the Aura Microwave Limb Sounder, Atmospheric Chemistry and Physics, 15, 2889–2902, doi:10.5194/acp-15-2889-2015, https://www.atmos-chem-phys.net/15/2889/2015/, 2015.

20 Murtagh, D.: SIW–Stratospheric Inferred Winds. Proposal in response to a Scientific Swedish Satellite based on the InnoSat Platform, Tech. rep., 2016.

Murtagh, D., Frisk, U., Merino, F., Ridal, M., Jonsson, A., Stegman, J., Witt, G., Eriksson, P., Jimenez, C., Mégie, G., de la Noë, J., Ricaud, P., Baron, P., Pardo, J., Hauchcorne, A., Llewellyn, E., Degenstein, D., Gattinger, R., Lloyd, N., Evans, W., McDade, I., Haley, C., Sioris, C., von Savigny, C., Solheim, B., McConnell, J., Strong, K., Richardson, E., Leppelmeier, G., Kyrola, E., Auvinen, H., and Oikarinen, L.:

25 An overview of the Odin atmospheric mission, Can. J. Phys., 80, 309, doi:10.1139/P01-157, 2002.

Newman, P. A., Coy, L., Pawson, S., and Lait, L. R.: The anomalous change in the QBO in 2015-2016, Geophysical Research Letters, 43, 8791–8797, doi:10.1002/2016GL070373, http://dx.doi.org/10.1002/2016GL070373, 2016GL070373, 2016.

Ochiai, S., Kikuchi, K., Nishibori, T., Manabe, T., Ozeki, H., Mizobuchi, S., and Irimajiri, Y.: Receiver Performance of the Superconducting Submillimeter-Wave Limb-Emission Sounder (SMILES) on the International Space Station, IEEE Transactions on Geoscience and

30 Remote Sensing, 51, 3791–3802, doi:10.1109/TGRS.2012.2227758, 2013.

Ochiai, S., Baron, P., Nishibori, T., Irimajiri, Y., Uzawa, Y., Manabe, T., Maezawa, H., Mizuno, A., Nagahama, T., Sagawa, H., Suzuki, M., and Shiotani, M.: SMILES-2 mission for temperature, wind, and composition in the whole atmosphere, SOLA, 13A, 13–18, doi:10.2151/sola.13A-003, 2017.

Olberg, M., Frisk, U., Lecacheux, A., Olofsson, A., Baron, P., Bergman, P., Florin, G., Hjalmarsson, A., Larsson, B., Murtagh, D., Olofsson,

35 G. , Pagani, L., Sandqvist, Aa. , Teyssier, D. , Torchinsky, S. A. , and Volk, K.: The Odin satellite - II. Radiometer data processing and calibration, A&A, 402, L35–L38, doi:10.1051/0004-6361:20030336, https://doi.org/10.1051/0004-6361:20030336, 2003.

Orsolini, Y. J., Limpasuvan, V., Pérot, K., Espy, P., Hibbins, R., Lossow, S., Larsson, K. R., and Murtagh, D.: Modelling the descent of nitric oxide during the elevated stratopause event of January 2013, Journal of Atmospheric and Solar-Terrestrial Physics, 155, 50 – 61, doi:https://doi.org/10.1016/j.jastp.2017.01.006, http://www.sciencedirect.com/science/article/pii/S1364682616302887, 2017.

Ortland, D. A., Skinner, W. R., Hays, P. B., Burrage, M. D., Lieberman, R. S., Marshall, A. R., and Gell, D. A.: Measurements of stratospheric winds by the High Resolution Doppler Imager, J. Geophys. Res., 101, 10 351–10 363, 1996.

Pérot, K., Urban, J., and Murtagh, D. P.: Unusually strong nitric oxide descent in the Arctic middle atmosphere in early 2013 as observed by Odin/SMR, Atmospheric Chemistry and Physics, 14, 8009–8015, doi:10.5194/acp-14-8009-2014, https://www.atmos-chem-phys.net/14/8009/2014/, 2014.

Pickett, H. M., Poynter, R. L., Cohen, E. A., Delitsky, M. L., Pearson, J. C., and Müller, H. S. P.: Submillimeter, millimeter and microwave spectral line catalog., J. Quant. Spectrosc. Ra., 60, 883–890, doi:10.1016/S0022-4073(98)00091-0, 1998.

Pumphrey, H. C., Read, W. G., Livesey, N. J., and Yang, K.: Observations of volcanic SO_2 from MLS on Aura, Atmospheric Measurement Techniques, 8, 195–209, doi:10.5194/amt-8-195-2015, https://www.atmos-meas-tech.net/8/195/2015/, 2015.

Rahnama, P., Gault, W. A., McDade, I. C., and Shepherd, G. G.: Scientific Assessment of the SWIFT Instrument Design, Journal of Atmospheric and Oceanic Technology, 30, 2081–2094, doi:10.1175/JTECH-D-12-00230.1, https://doi.org/10.1175/JTECH-D-12-00230.1, 2013.

Randall, C. E., Harvey, V. L., Singleton, C. S., Bailey, S. M., Bernath, P. F., Codrescu, M., Nakajima, H., and Russell, J. M.: Energetic particle precipitation effects on the Southern Hemisphere stratosphere in 1992?2005, Journal of Geophysical Research: Atmospheres, 112, n/a–n/a, doi:10.1029/2006JD007696, http://dx.doi.org/10.1029/2006JD007696, d08308, 2007.

Rothman, L., Gordon, I., Barbe, A., Benner, D., Bernath, P., Birk, M., Boudon, V., Brown, L., Campargue, A., Champion, J.-P., Chance, K., Coudert, L., Dana, V., Devi, V., Fally, S., Flaud, J.-M., Gamache, R., Goldman, A., Jacquemart, D., Kleiner, I., Lacome, N., Lafferty, W., Mandin, J.-Y., Massie, S., Mikhailenko, S., Miller, C., Moazzen-Ahmadi, N., Naumenko, O., Nikitin, A., Orphal, J., Perevalov, V., Perrin, A., Predoi-Cross, A., Rinsland, C., Rotger, M., Smith, M., Sung, K., Tashkun, S., Tennyson, J., Toth, R., Vandaele, A., and Auwera, J. V.: The HITRAN 2008 molecular spectroscopic database, Journal of Quantitative Spectroscopy and Radiative Transfer, 110, 533–572, doi:10.1016/j.jqsrt.2009.02.013, http://www.sciencedirect.com/science/article/pii/S0022407309000727, 2009.

Rüfenacht, R., Murk, A., Kämpfer, N., Eriksson, P., and Buelhler, S. A.: Middle-atmospheric zonal and meridional wind profiles from polar, tropical and midlatitudes with the ground-based microwave Doppler wind radiometer WIRA, Atmospheric Measurement Techniques, 7, 4491–4505, doi:10.5194/amt-7-4491-2014, http://www.atmos-meas-tech.net/7/4491/2014/, 2014.

Rüfenacht, R., Baumgarten, G., Hildebrand, J., Schranz, F., Matthias, V., Stober, G., Lübken, F.-J., and Kämpfer, N.: Validation of middle-atmospheric wind in observations and models, Atmospheric Measurement Techniques Discussions, 2017, 1–31, doi:10.5194/amt-2017-390, https://www.atmos-meas-tech-discuss.net/amt-2017-390/, 2017.

Sagawa, H., Sato, T. O., Baron, P., Dupuy, E., Livesey, N., Urban, J., von Clarmann, T., de Lange, A., Wetzel, G., Connor, B. J., Kagawa, A., Murtagh, D., and Kasai, Y.: Comparison of SMILES ClO profiles with satellite, balloon-borne and ground-based measurements, Atmospheric Measurement Techniques, 6, 3325–3347, doi:10.5194/amt-6-3325-2013, https://www.atmos-meas-tech.net/6/3325/2013/, 2013.

Sakazaki, T., Fujiwara, M., and Shiotani, M.: Representation of solar tides in the stratosphere and lower mesosphere in state-of-the-art reanalyses and in satellite observations, Atmospheric Chemistry and Physics, 18, 1437–1456, doi:10.5194/acp-18-1437-2018, https://www.atmos-chem-phys.net/18/1437/2018/, 2018.

Shepherd, G. G.: Development of wind measurement systems for future space missions, Acta Astronautica, 115, 206–217, doi:10.1016/j.actaastro.2015.05.015, http://www.sciencedirect.com/science/article/pii/S0094576515001976, 2015.

Stoffelen, A., Pailleux, J., Källén, E., Vaughan, J., Isaksen, L., Flamant, P., Wergen, W., Andersson, E., Schyberg, H., Culoma, A., Meynart, R., Endemann, M., and Ingmann, P.: The Atmospheric Dynamics Mission For Global Wind Field Measurement, Bull. Amer. Meteor. Soc., 86, 73–87, 2005.

Urban, J., Baron, P., Lautié, N., Schneider, N., Dassas, K., Ricaud, P., and De La Noë, J.: MOLIERE (v5): a versatile forward- and inversion model for the millimeter and sub-millimeter wavelength range, J. Quant. Spectrosc. Ra., 83, 529–554, doi:10.1016/S0022-4073(03)001040-3, 2004.

Urban, J., Lautié, N., Le Flochmoën, E., Jiménez, C., Eriksson, P., de La Noë, J., Dupuy, E., Ekström, M., El Amraoui, L., Frisk, U., Murtagh, D., Olberg, M., and Ricaud, P.: Odin/SMR limb observations of stratospheric trace gases: Level 2 processing of ClO, N_2O, HNO_3, and O_3, Journal of Geophysical Research: Atmospheres, 110, n/a–n/a, doi:10.1029/2004JD005741, http://dx.doi.org/10.1029/2004JD005741, d14307, 2005.

Waters, J. W., Froidevaux, L., Read, W. G., Manney, G. L., Elson, L. S., Flower, D. A., Jarnot, R. F., and Harwood, R. S.: Stratospheric ClO and ozone from the Microwave Limb Sounder on the Upper Atmosphere Research Satellite, Nature, 362, 597–602, 10.1038/362597a0, 1993.

Waters, J. W., Froidevaux, L., Harwood, R. S., Jarnot, R. F., Pickett, H. M., Read, W. G., Siegel, P. H., Cofield, R. E., Filipiak, M. J., Flower, D. A., Holden, J. R., Lau, G. K., Livesey, N. J., Manney, G. L., Pumphrey, H. C., Santee, M. L., Wu, D. L., Cuddy, D. T., Lay, R. R., Loo, M. S., Perun, V. S., Schwartz, M. J., Stek, P. C., Thurstans, R. P., Boyles, M. A., Chandra, K. M., Chavez, M. C., Chen, G.-S., Chudasama, B. V., Dodge, R., Fuller, R. A., Girard, M. A., Jiang, J. H., Jiang, Y., Knosp, B. W., LaBelle, R. C., Lam, J. C., Lee, K. A., Miller, D., Oswald, J. E., Patel, N. C., Pukala, D. M., Quintero, O., Scaff, D. M., Snyder, W. V., Tope, M. C., Wagner, P. A., and Walch, M. J.: The Earth observing system microwave limb sounder (EOS MLS) on the aura Satellite, IEEE Transactions on Geoscience and Remote Sensing, 44, 1075–1092, doi:10.1109/TGRS.2006.873771, 2006.

Wu, D. L., Schwartz, M. J., Waters, J. W., Limpasuvan, V., Wu, Q. A., and Killeen, T. L.: Mesospheric doppler wind measurements from Aura Microwave Limb Sounder (MLS), Advances In Space Research, 42, 1246–1252, 2008.

Wu, D. L., Yee, J.-H., Schlecht, E., Mehdi, I., Siles, J., and Drouin, B. J.: THz limb sounder (TLS) for lower thermospheric wind, oxygen density, and temperature, Journal of Geophysical Research: Space Physics, 121, 7301–7315, doi:10.1002/2015JA022314, http://dx.doi.org/10.1002/2015JA022314, 2015JA022314, 2016.